nature sustainability

Article

https://doi.org/10.1038/s41893-022-01024-1

Future socio-ecosystem productivity threatened by compound drought–heatwave events

Received: 14 July 2022

Accepted: 21 November 2022

Published online: 5 January 2023

Check for updates

Jiabo Yin[1] ✉, Pierre Gentine[2,3], Louise Slater[4], Lei Gu[5], Yadu Pokhrel[6], Naota Hanasaki[7], Shenglian Guo[1], Lihua Xiong[1] & Wolfram Schlenker[8]

Compound drought–heatwave (CDHW) events are one of the worst climatic stressors for global sustainable development. However, the physical mechanisms behind CDHWs and their impacts on socio-ecosystem productivity remain poorly understood. Here, using simulations from a large climate–hydrology model ensemble of 111 members, we demonstrate that the frequency of extreme CDHWs is projected to increase by tenfold globally under the highest emissions scenario, along with a disproportionate negative impact on vegetation and socio-economic productivity by the late twenty-first century. By combining satellite observations, field measurements and reanalysis, we show that terrestrial water storage and temperature are negatively coupled, probably driven by similar atmospheric conditions (for example, water vapour deficit and energy demand). Limits on water availability are likely to play a more important role in constraining the terrestrial carbon sink than temperature extremes, and over 90% of the global population and gross domestic product could be exposed to increasing CDHW risks in the future, with more severe impacts in poorer and more rural areas. Our results provide crucial insights towards assessing and mitigating adverse effects of compound hazards on ecosystems and human well-being.

Droughts and heatwaves are driven by complex interactions between physical processes and are often initiated by similar synoptic circulation anomalies[1,2]; they are thus likely to occur simultaneously[3,4]. As droughts are occurring more frequently and atmospheric warming triggers stronger land–atmosphere feedback, the risks of compound drought–heatwave (CDHW) events are intensified across the globe[5,6], amplifying adverse impacts on socio-economic sustainability and human well-being[7,8]. CDHWs can exacerbate vegetation mortality, for example, which in turn may cascade into other hazards, such as wildfires and crop yield losses[9–11]; they can also jeopardize electric grid reliability and adversely affect a wide range of natural and human-made systems[12]. In the United States alone, three CDHWs between 2011 and 2013 caused economic damages of roughly $60 billion[6].

How CDHWs regulate ecosystem productivity is also an important issue. The terrestrial biosphere acts as a prominent sink for anthropogenic CO_2, sequestering about 30% of annual CO_2 emissions[13,14].

[1]State Key Laboratory of Water Resources and Hydropower Engineering Science, Wuhan University, Wuhan, China. [2]Department of Earth and Environmental Engineering, Columbia University, New York, NY, USA. [3]Earth Institute, Columbia University, New York, NY, USA. [4]School of Geography and the Environment, University of Oxford, Oxford, UK. [5]School of Civil and Hydraulic Engineering, Huazhong University of Science and Technology, Wuhan, China. [6]Department of Civil and Environmental Engineering, Michigan State University, East Lansing, MI, USA. [7]Center for Climate Change Adaptation, National Institute for Environmental Studies, Tsukuba, Japan. [8]School of International and Public Affairs, Columbia University, New York, NY, USA. ✉e-mail: jboyn@whu.edu.cn;

However, climatic extremes can adversely affect its ability to function as a sink; for example, the 2003 European drought and heatwave reduced plant productivity by ~30%, thereby cancelling four years of CO_2 net uptake over Europe[15]. After severe CDHWs, plant recovery usually lags owing to reduced growth, non-reversible losses in hydraulic conductance or depletion of carbon reserves[16,17]. This lagged growth may in turn increase vulnerability to another CDHW if it occurs before complete recovery[8], potentially limiting the capacity of continents to act as carbon sinks[18,19].

With growing evidence about these damages, CDHWs are increasingly regarded as one of the worst climatic stressors to global socio-economic sustainability and ecosystem health[20–22]. Understanding CDHW dynamics in a warming Earth is thus essential for the implementation of the United Nations Sustainable Development Goals (SDGs), in particular SDG13, which aims to combat climate change and its impacts. Yet, how to describe CDHWs remains an open question, particularly in terms of defining a fully representative stress index[23]. Previous studies have assessed droughts through a variety of indices such as the (self-calibrated) Palmer Drought Severity Index and the soil moisture (SM) drought index[24]. More recently, terrestrial water storage (TWS), a key determinant of global water and energy budgets, has been employed to reveal large-scale drought impacts on hydrologic systems and plant growth. TWS represents the vertically integrated water storage as opposed to conventional indices that only capture partial water storages or fluxes[25,26]. However, the effects of TWS on future shifts in CDHW dynamics and the resulting impacts on socio-ecosystem productivity remain unexamined.

Here we present a quantitative assessment of the socio-economic and ecological consequences of CDHWs at a global scale, under both current and future climates. We first analysed the association between daily maximum near-surface temperature (T_{max}) and TWS from satellite observations, field measurements, and Gravity Recovery and Climate Experiment (GRACE)-constrained reconstruction and reanalysis data during 1979–2020. We detected strong multi-temporal-scale coupling during the warm season (Supplementary Fig. 1), highlighting the high likelihood of concurrent drought and heat extremes. To assess the physical mechanisms behind CDHWs, we measured the responses of large-scale and local-scale atmospheric dynamics to heat stress, drought and their temporally compounding extremes. We then evaluated the effects of climatic extremes on the terrestrial carbon budget by using net ecosystem productivity (NEP) as well as its partitioning into photosynthesis (that is, gross primary productivity (GPP)) and respiration (that is, total ecosystem respiration (TER)). We did this by employing in situ eddy-covariance flux tower observations, a recent satellite-based machine-learning-generated solar-induced chlorophyll fluorescence (SIF) dataset[27] and a light use efficiency theory-based GPP dataset[28]. Moreover, we assessed future shifts in CDHWs for various socio-economic and ecological subgroups using a large ensemble (96 scenarios) of climate–hydrology simulations under the Inter-Sectoral Impact Model Intercomparison Project Phase 2b (ISIMIP2b; Supplementary Table 1) and 15 members of TWS simulations by driving the H08 global hydrological model (GHM) with bias-corrected Coupled Model Intercomparison Project Phase 6 (CMIP6) ensemble outputs. Finally, we examined the changes in joint return period (JRP) using an 'AND' hazard scenario of CDHWs under a bivariate non-stationary framework, and we systematically quantified the associated uncertainty (more details are provided in the Methods).

Results

Observed water–heat–carbon dynamics in climatic extremes

Indicators of land water content (that is, TWS and SM) and T_{max} are negatively correlated globally (Fig. 1i and Extended Data Fig. 1), probably due to the increase in evapotranspiration during the warm season. The bimodality (that is, the binning distribution towards both ends) suggests that extreme stressors should not be assessed in isolation (Extended Data Fig. 1e–h) and can be explained by land–atmosphere coupling[29]. To disentangle the influence of atmospheric conditions on climatic extremes, we estimated the anomalies of composite variables during drought events, heat extremes and concurring CDHW events. Heat extremes (above the 90th percentile of T_{max}) occur under large-scale atmospheric conditions such as high convective available potential energy (CAPE) and high convective inhibition (CIN) co-occurring in higher-latitude regions (Fig. 1a,b). High CAPE suggests a high moist convection potential, thereby enhancing the likelihood of intense rainstorms. The moist convection potential over land is also linked to higher sensible heat flux, latent heat flux (upward positive) and column-integrated water vapour (CIWV), correlated with higher specific humidity (SH) over most lands in the Northern Hemisphere (Fig. 1c–f). Nevertheless, atmospheric moisture transport has weakened across almost the entire global land surface, as indicated by widespread negative anomalies of vertically integrated moisture convergence (VIMC), and thus decreases relative humidity (RH) over land (Fig. 1g,h). In the tropics and in several regions of the mid-latitudes, low CAPE is accompanied by high CIN and weak water–heat transport strength (negative anomalies of latent heat flux, CIWV, SH, VIMC and RH), which may enhance air dryness and thus propagate into terrestrial droughts (Fig. 1a–h). At higher latitudes and in dry conditions (as identified by a TWS-based drought severity index, TWS-DSI < −0.8; more details are provided in the Methods), we detected negative anomalies of CAPE, CIWV, SH and latent heat flux, which is opposite to the patterns found during extreme heat conditions (Supplementary Fig. 2). In the remaining land regions, the patterns of anomalies of water–heat variables are largely consistent with heat conditions, even though their responses to dry events are weaker than the responses to heat extremes. Due to these regionally divergent impacts of heat and dry extremes, the atmospheric conditions during concurrent hot–dry conditions generally indicate a more severe air dryness as well as less moist convection and water vapour transport, particularly in the mid-latitudes and tropics (Supplementary Fig. 3).

We then evaluated the impacts of these climatic extremes on the terrestrial carbon budget at global eddy-covariance tower sites (Supplementary Fig. 4 and Supplementary Table 2). We found a strong negative correlation between observed T_{max} and daily Global Land Data Assimilation System (GLDAS)-based TWS ($r = -0.2$, $P < 0.001$) (Fig. 1n), along with a bimodal behaviour (Fig. 1j). GPP responds to T_{max} both nonlinearly and non-monotonically: at low T_{max}, GPP is enhanced with rising T_{max} as it promotes photochemistry by warming[30,31]; however, when T_{max} is very high, further increases in

Fig. 1 | Anomalies of composite water–heat–carbon variables during extreme climatic events. a–h, Anomalies of CAPE (**a**), CIN (**b**), sensible heat flux (**c**), latent heat flux (**d**), CIWV (**e**), SH (**f**), VIMC (**g**) and RH (**h**) during extreme heat events. The extreme heat events in **a**–**h** are identified using the 90th percentile of ERA5 T_{max} in each grid cell. **i**, Pearson's correlation coefficient (r) between daily GLDAS TWS and ERA5 T_{max}. **j**, Mean probability of each percentile bin of T_{max} and daily GLDAS TWS across 73 flux tower sites. **k**–**m**, Mean anomalies of GPP (**k**), TER (**l**), and NEP (**m**) for each percentile bin of T_{max} and GLDAS TWS across 73 flux tower sites. These three panels share the same colour bar. **n**, Pearson's correlation coefficient between T_{max} and TWS (or SM) from different datasets across 73 flux tower sites. JPL, Jet Propulsion Laboratory; CSR, Center for Space Research; GSFC, Goddard Space Flight Center. **o**, Anomalies of GPP, TER and NEP above 90th percentiles of T_{max} and below 10th percentiles of daily TWS (or SM) across 73 flux tower sites. The daily TWS in **j**–**m** and the box plot in **o** are from the GLDAS-2.2 dataset. In **n**,**o**, the mean values of different datasets are marked by different shapes, and the centre lines indicate the median values; the box bounds indicate the 25th/75th percentile values, and the whiskers indicate the minimum/maximum values. At each site/grid, anomalies of the variables are calculated as the difference between the daily values in extreme events and the mean daily values in the five-month warm season.

https://doi.org/10.1038/s41893-022-01024-1

T_{max} cause GPP stress (Fig. 1k), which strongly inhibits plant photosynthesis[32]. TER increases with T_{max} but at a more moderate pace than GPP (Fig. 1l), so that net ecosystem exchange still responds negatively to the highest T_{max} (Fig. 1m). TWS depletion might reduce GPP and TER, as water stress reduces photosynthesis through stomatal and non-stomatal regulation and respiration through soil

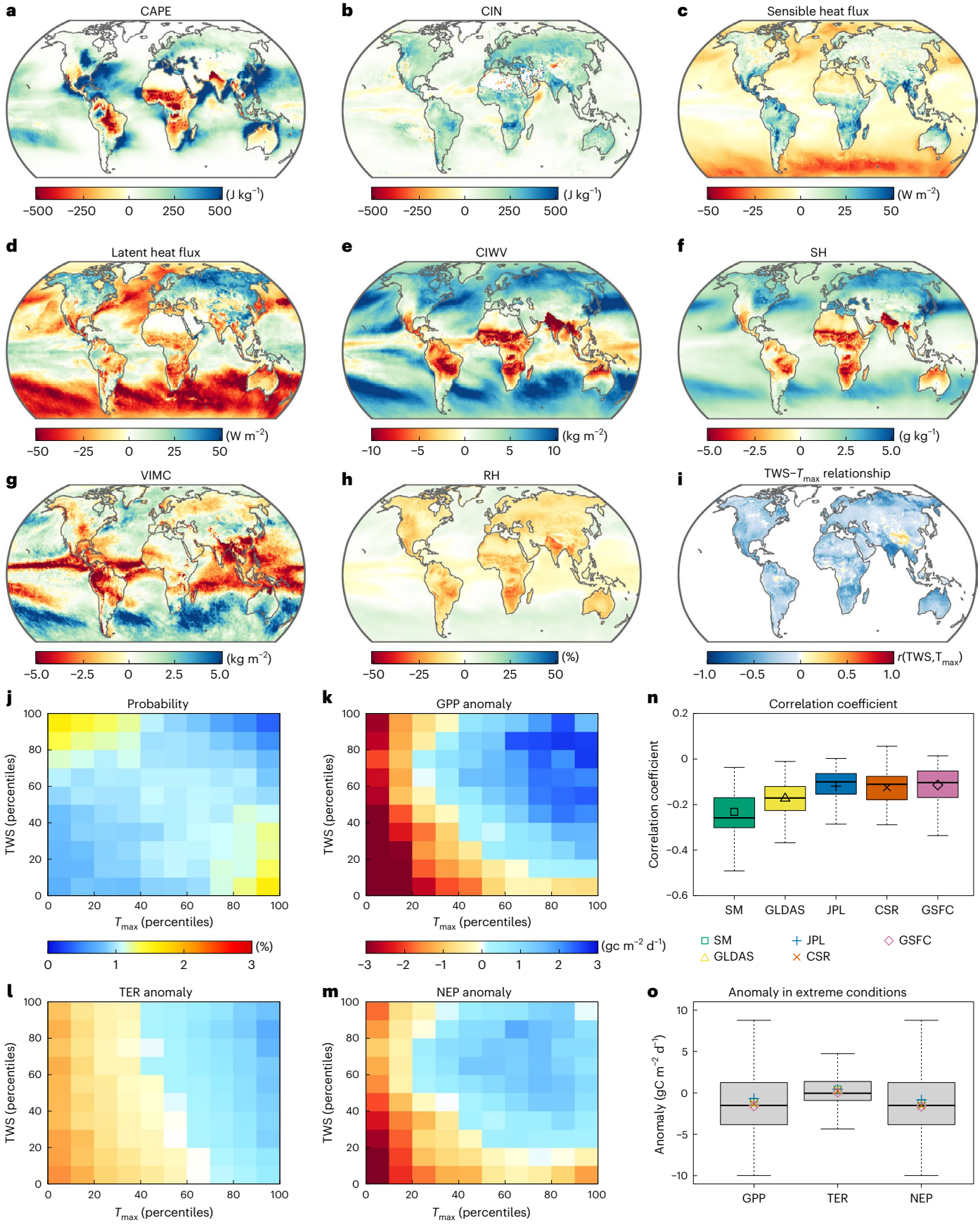

https://doi.org/10.1038/s41893-022-01024-1

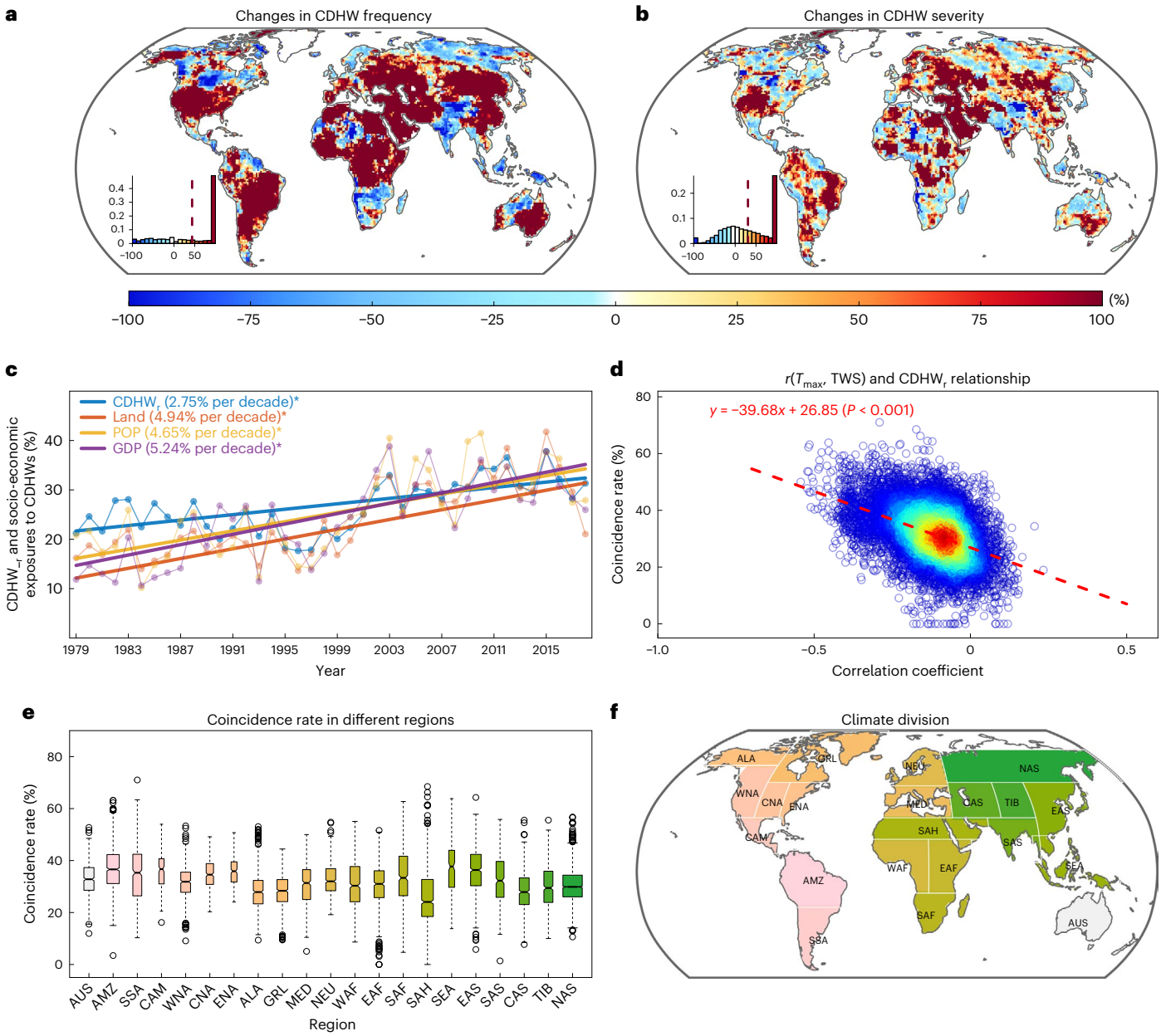

Fig. 2 | Recent changes in frequency and intensity of CDHWs as well as related socio-economic exposure. a,**b**, Changes in frequency (**a**) and severity (**b**) of CDHWs between two periods (recent, 1999–2019, minus past, 1979–1998). The insets in **a**,**b** show the histogram of the relative change percentages, with the dashed vertical line representing the mean value. **c**, Temporal dynamics of the global average CDHW$_f$ and the fraction of land area (Land), population (POP) and GDP that is exposed to CDHWs. The asterisks indicate that the change is significant ($P < 0.05$) as detected by the Mann–Kendall test. **d**, Relationship between $r(T_{max}$, TWS) and CDHW$_f$ across the land grids (excluding Greenland and Antarctica); the two-sided F-test was used for testing significance. **e**,**f**, Box plots of coincidence rates (**e**) in 21 different Giorgi climate regions (**f**). In the box plots in **e**, the centre line indicates median value, the box bounds indicate the 25th/75th percentile values, the whiskers indicate the minimum/maximum values and the circles indicate the outliers. The droughts are identified by reconstructed TWS data, and the heatwaves are detected by using T_{max} from the Berkeley Earth Surface Temperatures (BEST) dataset. AUS, Australia; AMZ, Amazon Basin; SSA, Southern South America; CAM, Central America; WNA, Western North America; CAN, Central North America; ENA, Eastern North America; ALA, Alaska; GRL, Greenland and Northern Territories; MED, Mediterranean Basin; NEU, Northern Europe; WAF, Western Africa; EAF, Eastern Africa; SAF, Southern Africa; SAH, Sahara; SEA, Southeast Asia; EAS, East Asia; SAS, South Asia; CAS, Central Asia; TIB, Tibet; NAS, North Asia.

enzyme activities. Under concurrent high T_{max} and low TWS, NEP mean anomalies (−1.42 gC m^{-2} d^{-1}) are largely determined by GPP anomalies (−1.25 gC m^{-2} d^{-1}), while TER is slightly increased with a mean anomaly of 0.30 gC m^{-2} d^{-1} (Fig. 1o). When assessing these same relationships using in situ root-zone SM as well as monthly TWS from three GRACE/GRACE-FO solutions, we still detected impairing effects of heat and dry extremes on terrestrial carbon uptake (Fig. 1o and Extended Data Fig. 2). The machine-learning-generated SIF and MODIS-retrieved GPP anomalies are negative in most regions during extreme heat, drought and concurrent extremes (Extended Data Fig. 3), except in boreal regions and small areas of tropical rainforests such as the Amazon forests, where SIF and GPP are enhanced because ecosystems tend to be temperature limited[29,33]. The potential for heat- or dryness-related carbon loss therefore needs to be understood when exploring the impacts of concurrent extreme climatic events on ecosystems.

Observed increases in climatic extremes and their impacts

Recent changes in climatic extremes are evaluated in terms of their frequency, days, duration and severity (see the definitions in the Methods). Globally, the frequencies of the three types of climatic extreme events (heatwave, drought and CDHW) are increasing; for example, 67% of global land areas have experienced more CDHWs in recent decades (Fig. 2a). The duration and severity of CDHWs are greatly increasing in the eastern United States, central South America, parts of central Africa, eastern Europe, the Middle East and parts of eastern Asia (Fig. 2b and Supplementary Fig. 5). Furthermore, the global average coincidence rate (that is, the ratio of CDHW to heatwave events ($CDHW_r$), 2.75% per decade), exposed land area (4.94% per decade), exposed population (4.65% per decade) and exposed gross domestic product (GDP) (5.24% per decade) have all significantly increased since 1979 (Fig. 2c). Eight of the Giorgi climate regions are identified as CDHW hotspots (that is, AMZ, CAM, ENA, CNA, MED, SSA, NAS and EAS; see the locations in Fig. 2f), where CDHWs have both long duration and severe magnitude (Supplementary Fig. 6). The hotspots are located in areas with high $CDHW_r$, where heatwaves and droughts have a high likelihood of occurring simultaneously and are accompanied by stronger negative r(TWS, T_{max}) (Fig. 2d,e). Five (three) out of eight hotspots show significant (insignificant) increases in socio-economic (either GDP or population-weighted) exposure due to exacerbated CDHWs (Extended Data Fig. 4 and Supplementary Fig. 7); some regions even show increasing rates of >10% per decade for both GDP and population exposure. The three GRACE/GRACE-FO solutions detect similar hotspots to the reconstructed data (Supplementary Figs. 8–10) but indicate stronger trends and socio-economic exposures (Supplementary Figs. 11–13), which may be driven by more rapid intensification of warming and drying in the past decade, implying that tackling and adapting to these climatic hazards is a growing societal challenge.

A comparison of the coupled TWS-DSI with traditional drought indices suggests that the TWS-DSI provides new information and a stronger signal of drought exacerbation in recent decades. Unlike the standardized runoff index, which is highly correlated with the standardized precipitation index, the TWS-DSI exhibits substantial changes over time in most of the Giorgi regions (Supplementary Figs. 14–16), because it encompasses all surface and subsurface storage components that are relevant to terrestrial water availability. The TWS-DSI also differs from the standardized precipitation evapotranspiration index (SPEI) and SM-based indices, which fail to characterize real conditions of soil and groundwater (surface water storage such as ice and snow) (Supplementary Figs. 17–19). The TWS-DSI suggests that the drought magnitudes have substantially changed across most Giorgi regions in recent decades, while the other indices show negligible changes between the recent and past periods, thus underestimating drought intensification in most subregions and at the global scale. This considerable difference between the abilities of different indices to estimate temporal changes underscores the importance of considering groundwater and human activities in assessing drought risks[26,34], by using an integrated index such as the TWS-DSI.

Projections of climatic extremes and socio-ecosystem effects

Before projecting future CDHW characteristics, we first evaluated the anomalies of composite water–heat–carbon variables during extreme climatic events, under historical and future periods (Supplementary Figs. 20–22, Supplementary Text 1 and Fig. 3). RH is globally decreasing and surface downwelling short-wave and long-wave radiation are globally increasing, both with stronger rates during CDHWs than during individual climatic extremes. In contrast, the SH anomalies are not globally consistent and display a different sign in the tropics and other land regions (Fig. 3a–l). Heat-extreme GPP anomalies are negative in most regions except in the water-limited boreal regions (Supplementary Fig. 20m–o). TER is greatly enhanced in boreal regions but slightly reduced over most other regions between 50° S and 50° N, in agreement with flux tower sites (Supplementary Fig. 20p–r and Fig. 1l), which are mostly located in the mid and low latitudes (Supplementary Fig. 4). The negative effect of extreme low TWS on GPP significantly exceeds the effect of extreme high T_{max} in future simulations over more than 80% (75%) of land areas under Representative Concentration Pathway (RCP) 8.5 (RCP6.0), highlighting the increasing importance of water limitation for future carbon assimilation (Supplementary Figs. 20–22m–u). We also project the anomalies of GPP, TER and NEP using the Community Land Model (CLM4.5) forced by bias-corrected GFDL-ESM2M climate data, and these independent evaluations corroborate the increasing constraining role of limited water availability for the future carbon sink (Extended Data Fig. 5 and Supplementary Fig. 23). During concurrent heat and drought conditions, photosynthesis and respiration are both reduced, as detected by strong negative anomalies of GPP, TER and NEP in most global land areas except for the boreal high latitudes (Fig. 3m–u), implying large reductions in ecosystem carbon uptake in a future warmer climate.

Negative NEP anomalies under CDHWs are much stronger than when considering only one extreme, particularly under future climate (Fig. 3, Supplementary Figs. 20–23 and Extended Data Fig. 5). The projected reductions in carbon uptake during compounding drought–heat events occur alongside general increases in global productivity from CO_2 fertilization[35,36]. This paradox may be explained by the fact that the CO_2 fertilization effect on GPP is offset by the increase in compound events in some regions (for example, the Amazon region and southern Europe)[19], where the respiration losses lead to lower future NEP than in historical simulations with minimal projected increases in GPP. Vegetation mortality and subsequent regrowth and succession processes are usually poorly simulated by Earth system models (ESMs). If large drops in productivity driven by extreme events lead to enhanced vegetation mortality, the effects of climatic extremes on terrestrial productivity and carbon storage may be greater than those simulated by ESMs[37].

The occurrence of CDHWs is projected to increase fourfold over half of the global landmasses (Fig. 4a–c), and the number of CDHW days is projected to increase sixfold in 68% of the globe under all RCPs (Extended Data Fig. 6). Almost 70% of global land areas are projected to experience a fourfold intensification of CDHW duration and severity under the medium- and high-emission pathways (that is, RCP6.0 and RCP8.5), while RCP2.6 suggests a weaker (that is, twofold) intensification rate (Fig. 4d–f and Extended Data Fig. 6). Generally, the intensification is greatest for CDHWs, followed by heatwaves, then droughts, which suggests that heatwaves may play a dominant role in exacerbating future CDHWs (Fig. 4, Extended Data Fig. 6 and Supplementary Fig. 24). The increased $CDHW_r$ indicates that the interdependence between heatwaves and droughts is growing as the climate warms (Fig. 4g). The fractions of the global land area, population and GDP exposed to CDHWs are generally projected to increase until the late twenty-first century (Fig. 4h–j). Under RCP2.6, the global land area exposed to CDHWs increases from 18% during the baseline period to 34% by the end of the twenty-first century, while the exposed global fractions of population and GDP increase from 19% and 18%, respectively, to ~36% each by the 2070s and then slightly decrease to 31% and 30%, respectively,

Fig. 3 | Anomalies of water, heat and carbon fluxes due to concurrent hot–drought conditions during historical and future periods as estimated by climate models. a–l, Anomalies of RH (**a–c**), SH (**d–f**), surface downwelling short-wave radiation (SR) (**g–i**) and long-wave radiation (LR) (**j–l**) during CDHWs. **m–u**, Anomalies of GPP (**m–o**), TER (**p–r**) and NEP (**s–u**) due to high monthly T_{max} (above the 90th percentile) and low TWS (TWS-DSI < −0.8). Anomalies of RH, SH, SR and LR (GPP, TER and NEP) are calculated as the difference between daily (monthly) values in concurrent hot–drought conditions and the mean values during the entire warm season. Stippling denotes regions where the sign of the relative changes is consistent with the sign of the multi-model means (as shown in the figure) in at least 80% of ESM–THM combinations. The historical anomalies (left column) combine historical and RCP6.0 TWS data to estimate the TWS-DSI.

https://doi.org/10.1038/s41893-022-01024-1

by end of this century. Under RCP6.0 (RCP8.5), substantial increases are projected in CDHW exposure, global fractional land area, population exposure and GDP exposure, from ~17% (16%) during the baseline period to 40%, 38% and 41% (38%, 36% and 36%), respectively. Overall, an additional 17–21% of the global population and 18–25% of the GDP are projected to be exposed to CDHWs in future climates, which translates

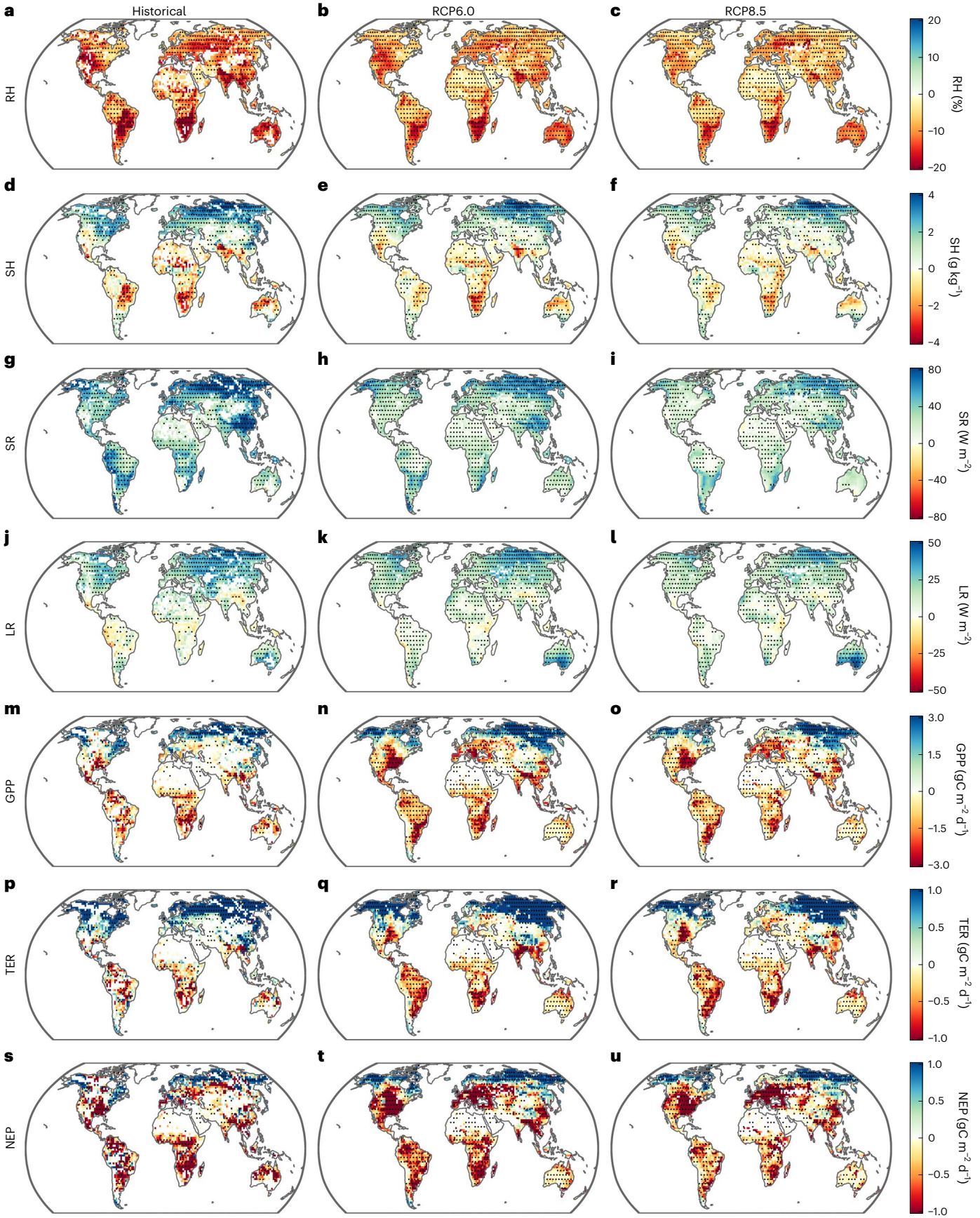

https://doi.org/10.1038/s41893-022-01024-1

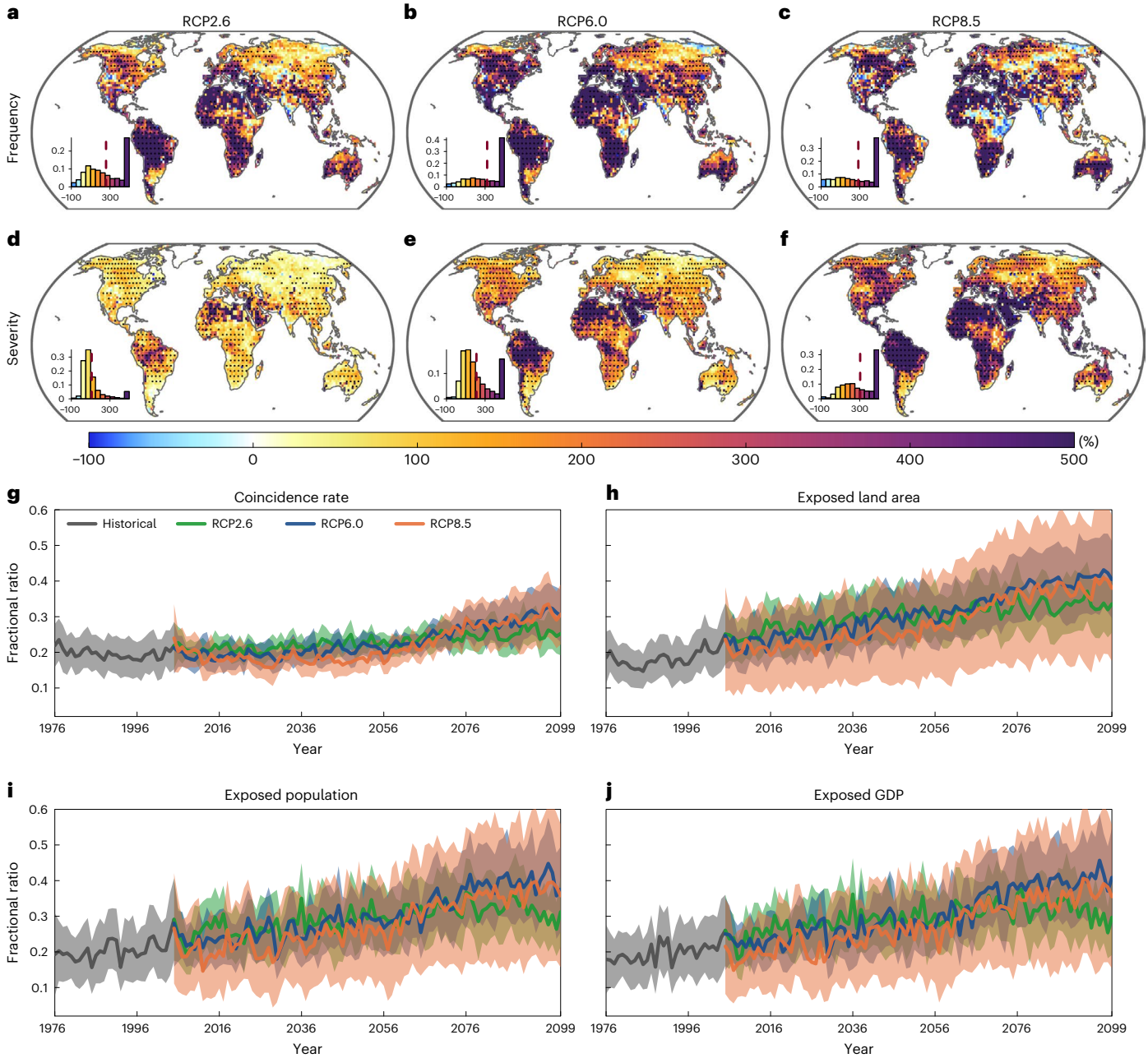

Fig. 4 | Future changes in the characteristics of CDHWs and socio-economic exposure to CDHWs under model simulations. a–f, Relative changes in the frequency (**a**–**c**) and severity (**d**–**f**) of CDHWs from the historical period to the future period. The insets in show the histograms of the relative change percentages, with the dashed vertical line representing the mean value. Stippling denotes regions where the sign of the relative changes is consistent with the sign of the multi-model means (as shown in the figure) in at least 80% of the GCM–THM models. **g–j**, Temporal dynamics of the global average coincidence rate (**g**), exposed land area (**h**), exposed population (**i**) and exposed GDP (**j**). The shading represents ±1 s.d., and the historical exposures are presented only by combining historical and RCP2.6 TWS data in estimating the TWS-DSI. These results are derived from the ISIMIP2b multiple impacts model ensemble.

to an additional ~1.4 billion to ~1.7 billion people and ~US$13 trillion to ~US$20 trillion (at 2015 purchasing power parity) per year. With TWS simulated by the H08 model forced by five bias-corrected CMIP6 models under three Shared Socio-economic Pathways (SSPs) (see the details in the Methods), we found stronger exacerbation of CDHWs and associated socio-economic exposure than the CMIP5-oriented projections, accompanied by a reduced uncertainty (Extended Data Fig. 7 and Supplementary Fig. 25).

Future bivariate risks of CDHWs and associated uncertainty

Under RCP8.5, the JRPs of the historical 50-year CDHW (as measured during the period 1976–2005) are projected to be below 10 years in more than 85% of global land areas (or 52% and 75% under RCP2.6 and RCP6.0). We found high inter-model agreement, implying that the occurrence of CDHW extremes will be at least fivefold globally by the end of this century (Fig. 5d and Supplementary Fig. 26a–c). Most hotspots might even experience a tenfold intensification of CDHW occurrence by the end of the century, as the historical 50-year CDHW is projected to occur once every 5 years by then under RCP8.5. Similarly, the three RCP scenarios project that over 90% of the population and GDP in most global land areas will be exposed to increasing CDHW risks by the end of this century (Supplementary Fig. 26d–i). Moreover, the exposed land area, population and fraction of global GDP are all increasing as the climate warms, with the global average fraction of land area exposed to the

https://doi.org/10.1038/s41893-022-01024-1

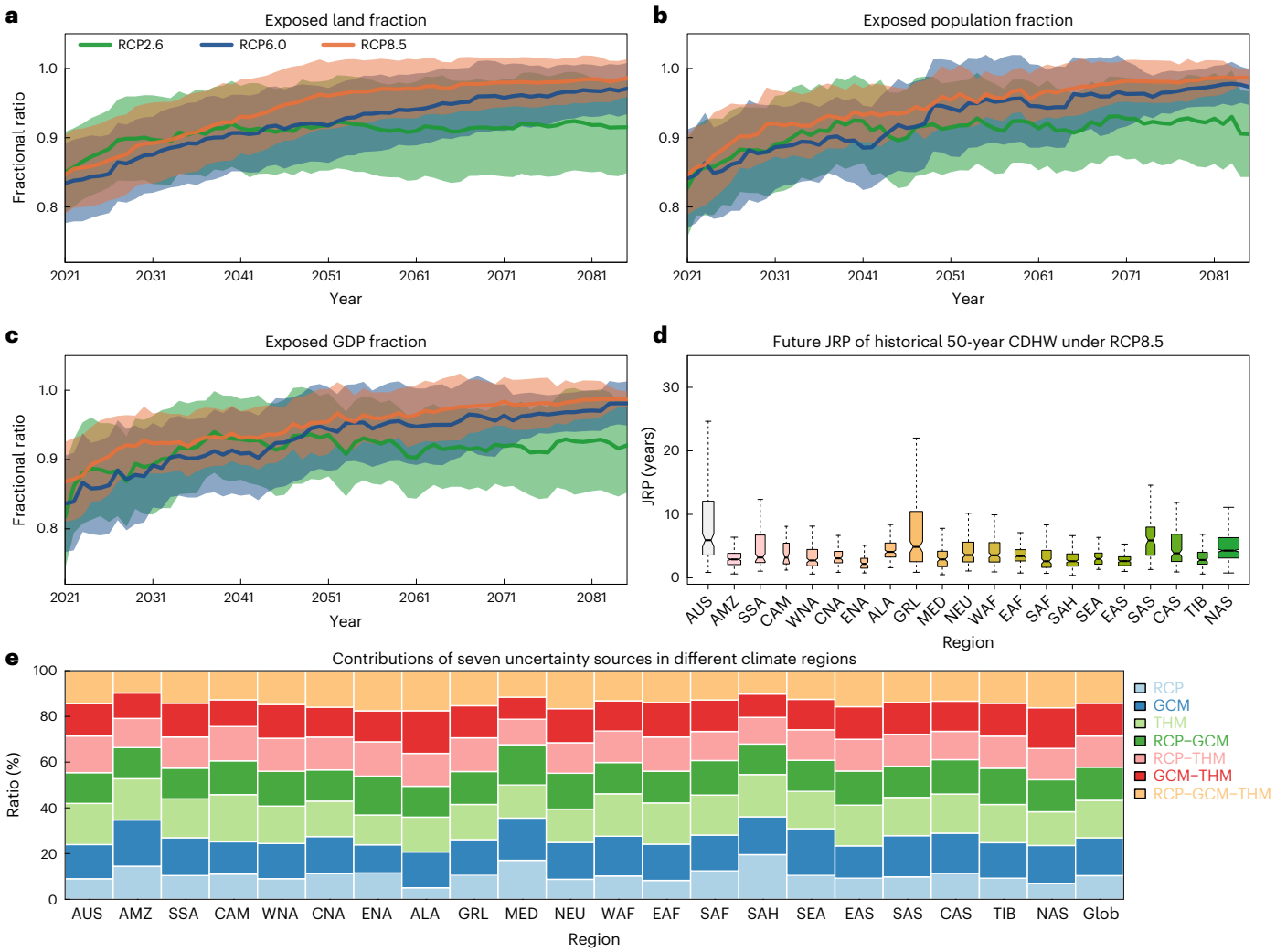

Fig. 5 | Projected JRP of historical 50-year bivariate CDHWs and socio-economic exposure. a–c, Temporal dynamics of the fractions of global average exposed land area (**a**), population (**b**) and GDP (**c**) due to increasing CDHW risk; the solid curves and shading indicate the multi-model means ± s.d. **d**, Box plots of the updated JRP of the historical 50-year CDHW in different Giorgi climate regions under RCP8.5; the centre line indicates the median value, the box bounds indicate the 25th/75th percentile values and the whiskers indicate the minimum/maximum values. **e**, Average contribution ratios of seven uncertainty sources in different Giorgi climate regions and the global landmass (Glob). These results are derived from the ISIMIP2b multiple impacts model ensemble.

historical 50-year CDHW increasing from about 82% to nearly 100% by end of this century (Fig. 5a–c). The CMIP6-based ensemble simulations from H08 indicate even higher bivariate risks of CDHWs, as the fractions of population and GDP that are exposed might approach 100% with smaller uncertainty by 2100, and the average JRP of the historical 50-year CDHW is projected to be below the 5-year return period across almost all the climate regions under SSP585, suggesting a tenfold intensification (Extended Data Fig. 8a–m).

Last, we decomposed the overall uncertainty into different components of seven different sources for CMIP5-based projections (or three sources for CMIP6-based projections) at the global scale by using the multivariate analysis of variance (MANOVA) method (Methods). The uncertainty contribution ratios vary across different regions, due to the different RCPs and terrestrial hydrological models (THMs) (Supplementary Fig. 26j–p and Extended Data Fig. 8n). For example, in the Amazon forests, the RCPs and THMs induce ~27% and 22% of the overall uncertainty, respectively. The interactions between scenarios, global climate models (GCMs) and THMs also play an important role (Fig. 5e) and reveal the importance of examining CDHW changes by using a large climate-scenario ensemble and exploring the interactions of different models for projecting future climatic extremes.

Discussion

Large-scale atmospheric anomalies (blocking, subsidence and free tropospheric warming) play a key role in the coupling of T_{max} and TWS, and they have been recognized as important drivers of the onset and development of droughts and heatwaves[38–40]. The strong coupling of T_{max} and TWS suggests that the impacts of associated extremes (that is, heatwaves and droughts) should not be assessed in isolation. Compound droughts and heat extremes reduce terrestrial carbon uptake much more strongly than either of the two in isolation. The decline in carbon uptake induced by compound extreme events could be partially offset by CO_2 fertilization effects in the future[19], but this offset does not occur in most regions in the projections by models. Climate models project increases in the negative effects of compound extreme events on NEP such that, despite CO_2 fertilization effects, future NEP during compound extreme events remains unchanged or decreases slightly in reference to historical conditions, especially in the Amazon and southern Europe. Our large climate–hydrology model ensemble under both CMIP5 and CMIP6 projects that CDHW magnitudes (occurrence, duration and severity) will quadruple in 70% of global land areas under medium- and high-emission scenarios. The $CDHW_r$ is also increasing globally, indicating that the interdependence between heatwaves and

droughts is strengthening as the climate warms. Importantly, we found that the frequency of extreme CDHWs (historical 50-year events) will increase tenfold under the highest-emission scenario, and over 90% of the world population and GDP is projected to be exposed to increasing bivariate CDHW risks in the future climate under all SSPs and RCPs.

As poor people often live in risky areas and have limited capacity to adapt, they might be more exposed or more vulnerable to natural disasters than wealthier people[41,42]. Numerous studies have reported that climate change might have unequal impacts on people with different levels of annual income[43,44]. We therefore examined whether the CDHW risks and corresponding socio-economic exposure are different between poorer and richer subgroups (refer to Supplementary Text 2 for identification). Focusing on the bottom and top quintiles (that is, grid cells where the GDP per capita is below the 20th percentile or above the 80th percentile in each climate region), we found that the poorer areas have a higher fraction of the population and GDP (0.44 and 0.44, respectively) exposed to CDHWs than the richer areas (0.39 and 0.38, respectively) by 2070–2099 under SSP585 (Extended Data Fig. 9). Poorer people in most Giorgi regions (for example, AUS, EAS and TIB) are more vulnerable to CDHWs than wealthy people in terms of higher $CDHW_r$ and socio-economic exposure. These disproportionate effects are not found in a few other regions (for example, AMZ and NEU), suggesting that regional complexity should be considered when designing climate mitigation policies. Similarly, people in urban areas are generally more capable of adapting, mitigating and insulating themselves and their livelihoods from the effects of CDHWs, relative to rural populations. We therefore also compared the CDHW risks in rural versus urban areas, which are defined by using the bottom and top quintiles of population density in each region (Supplementary Text 2). Rural areas are projected to face higher $CDHW_r$ and higher GDP and population exposures than urban areas under climate change across all SSPs (Supplementary Fig. 27). When the rural/urban (or poor/rich) areas are defined by using a more extreme threshold (that is, the 10th/90th percentile values), the effects of CDHWs are even more disproportionate (Supplementary Figs. 28 and 29), suggesting that poorer people currently live in marginal areas that are more exposed to extreme climatic conditions. We should note that our analysis keeps the definition of bottom quintile for GDP per capita and population density fixed at the 2015-year level and therefore does not consider human migration or regional GDP changes. The distribution of poor and rural regions might shift under climate change (Extended Data Fig. 10 and Supplementary Fig. 30), and the ultimate societal impact of CDHWs is a function of the exposure and vulnerability of various groups. In future works, human management and vulnerability should be considered in different regions to understand the impacts of CDHWs on socio-economic systems. Nevertheless, our findings provide a firm conclusion that future CDHW hazards are projected to intensify significantly and challenge the sustainable development of future socio-ecosystems. This work thus calls for stark mitigation and adaptation actions to reduce the adverse impacts of warming on societies and to sustain ecosystem productivity, easing the growing pressures on global sustainable development, particularly for poorer and more rural areas.

Methods

Models, simulation settings and forcing data

The large ensemble simulations include 96 scenario–model combinations from CMIP5 and 15 combinations from CMIP6. The CMIP5-based projections include three emission scenarios (that is, RCPs 2.6, 6.0 and 8.5), four GCMs and eight THMs. The eight THMs include six GHMs, CWatM, H08, MPI-HM, PCR-GLOBWB, WaterGAP2 and WaterGAP2-2c; one global land surface model, CLM4.5; and one dynamic global vegetation model, LPJmL. All models simulate the key terrestrial hydrological (for example, soil, vegetation and river) processes (see the details in Supplementary Table 3), which are forced by the ISIMIP2b daily meteorological forcing data[45] from four GCMs under CMIP5 (Supplementary Table 1). For each GCM, we used both bias-corrected outputs and the TWS simulations from eight THMs, which cover both the historical baseline (1976–2005) and the future projections (2006–2099). To improve the robustness of the future projections, we also used TWS simulated by the H08 model forced by outputs from five CMIP6 GCMs (that is, M6A-LR, GFDL-ESM4, MPI-ESM1-2-HR, MRI-ESM2-0 and UKESM1-0-LL) under three SSPs (SSP126, SSP370 and SSP585), which have been systematically bias-corrected under ISIMIP3b[46]. To assess the projected impacts of climatic extremes on ecosystem productivity, we also used the GPP, autotrophic respiration and heterotrophic respiration outputs from the CLM4.5 model under historical conditions and two RCPs (RCP2.6 and RCP6.0), which is forced by bias-corrected GFDL-ESM2M outputs. We deduced TER by summing autotrophic respiration and heterotrophic respiration and then calculated NEP by subtracting TER from GPP. We also used the GPP, TER and NEP of the outputs from GFDL-ESM2M, HadGEM2-ES and IPSL-CM5A-LR (not available in MIROC5). All simulations were conducted at a spatial resolution of 0.5° × 0.5°, but the results were bilinearly interpolated to a spatial resolution of 2° × 2° for a robust projection. In each model grid cell, we defined the warm season as the five-month period with the highest mean T_{max} in the historical period.

GRACE/GRACE-FO and reconstructed TWS datasets

TWS anomalies from GRACE/GRACE-FO satellite measurements were used to evaluate global terrestrial droughts for the 2002–2020 period. We used the latest mascon products from three processing centres: the Jet Propulsion Laboratory of the California Institute of Technology, the Center for Space Research at the University of Texas at Austin and the National Aeronautics and Space Administration's Goddard Space Flight Center. To consider possible uncertainty sourced from different processing procedures, we used the GRACE/GRACE-FO ensemble mean TWS anomalies by calculating the average time series of the three mascon datasets. To provide a long-term evaluation of climatic extremes, we also used observation-constrained monthly TWS data with a resolution of 0.5° × 0.5° covering 1979–2019, which is constructed by training a statistical model with multi-source satellite and reanalysis datasets[47]. Based on two different GRACE products and three different meteorological forcing datasets, this reconstructed dataset consists of six reconstructed products of 100 ensemble members each, which has been well validated over 90 large (>500,000 km^2) river basins and annual streamflow series from 12,496 small (<10,000 km^2) basins. We averaged all six products to develop an ensemble mean reconstructed TWS. To assess different drought indices, we also used the global 0.5° × 0.5° SPEI data for 2002–2020 from the Climatic Research Unit version 2.6. In addition, we used the daily 0.25° × 0.25° TWS data for 2003–2020 from the Catchment Land Surface Model simulation under GLDAS-2.2.

Reanalysis and Global Land Evaporation Amsterdam Model data

We used the hourly CAPE, CIN, CIWV, surface sensible heat flux, latent heat flux, 2 m air temperature (T_{2m}), 2 m dew point temperature (T_{dew}) and air pressure (pr) from the fifth-generation atmospheric reanalysis of the European Centre for Medium-Range Weather Forecasts (ERA5, 1979–2020). First, the 2 m hourly RH was computed on the basis of T_{2m} and T_{dew}, and the 2 m SH was derived by T_{dew} and pr. We then derived T_{max} and daily average values of the other variables. We also used the global gridded T_{max} data for 1979–2019 from BEST, which incorporates approximately 39,000 land stations. To identify the droughts by different indices, we used the monthly root-zone (0–100 cm) SM, precipitation and runoff from ERA5. We also used the daily root-zone SM for 1980–2020 from the Global Land Evaporation Amsterdam Model (GLEAM) version 3.5a. In the observational analysis, the results of all the different gridded datasets were bilinearly interpolated to a spatial resolution of 1° × 1°. We evaluated climatic extremes only in

the warm season because heat-related morbidity and mortality in the summer tend to exert the more severe impacts on socio-ecosystems. We therefore defined the warm season as the hottest five months of the climatology of the ERA5 T_{max} for each grid cell (Supplementary Fig. 1).

FLUXNET2015 data

We used half-hourly temperature, SM, GPP, TER and NEP data from the FLUXNET2015 dataset. SM is measured as the volumetric soil water content (percentage) at all available depths. These data were processed following a consistent and uniform processing pipeline. We used temperature and SM that were gap-filled using the marginal distribution method[48]. NEP was obtained using a variable friction velocity (u^*) threshold for each year, with references selected on the basis of model efficiency, and was partitioned into GPP and TER following the night-time partitioning method[49]. We selected 73 sites (830 site years) with data covering no less than three years (Supplementary Table 2 and Supplementary Fig. 4). Daytime half-hourly data (7:00 to 19:00) in the warm season were aggregated to daily values. The warm season is defined as days when running seven-day mean temperatures are higher than the 60th percentile of daily temperature for the site. We also used a machine-learning-constrained SIF dataset and a MODIS-retrieved GPP dataset[27,28]. The SIF dataset was generated by training a machine learning algorithm on the basis of Orbiting Carbon Observatory-2 (OCO-2) SIF observations and surface reflectance from the MODIS. This dataset can capture the seasonal and spatial variability of raw OCO-2 SIF at the far-red band (767 nm), which has been demonstrated to strongly relate to spatiotemporal variation of GPP[27]. In this study, we used the clear-sky daily SIF for 2000–2020 with a four-day temporal resolution and a 0.5° spatial resolution. The retrieved GPP dataset is based on an improved light use efficiency theory and is driven by satellite data from MODIS and climate data from NCEP Reanalysis II, and it has moderate spatial (500 m) and temporal (eight-day) resolutions over the entire globe for 2000–2019[28].

Socio-economic data

For the analysis of the global socio-economic index affected by historical (1979–2020) climatic extremes, we used the global gridded 2015 population data from the Socioeconomic Data and Applications Center at Columbia University. These population data are consistent with national censuses and have been adjusted to match the 2015 Revision of the United Nations' World Population Prospects country totals, which are produced at 30-arcsecond (~1 km at the Equator) resolution. We also used a global gridded 2015 GDP dataset at a 30-arcsecond resolution, which was produced by fully making use of all available subnational data and the World Bank dataset[50]. To project future global exposure of populations and assets to climatic extremes, we employed a spatially explicit global dataset produced by employing population and urbanization projection models and the Cobb–Douglas production model[51]. This dataset includes gridded population and GDP data under five SSPs, covering 2010–2100 at a spatial resolution of 0.5° × 0.5°, and has been widely used in climate change impact assessments[34]. Considering the socio-economic challenges to mitigation by different development roads, the RCP2.6 (RCP6.0) scenario is associated with SSP1 (SSP4), while the RCP8.5 is associated with SSP5 (ref. 52).

Deriving near-surface RH and SH

As near-surface RH and SH are not available in the ERA5 dataset, they were calculated by using T_{2m}, T_{dew} and pressure. The Clausius–Clapeyron relationship can describe the relationship between saturation vapour pressure (e_{sat}) and temperature (T)[52]:

$$e_{sat}(T) = e_{s0} \exp\left[\frac{L_v}{R_v}\left(\frac{1}{T_0} - \frac{1}{T}\right)\right] \quad (1)$$

where $T_0 = 273.16$ K and $e_{s0} = 611$ Pa are integration constants; and L_v and R_v refer to the latent heat of vaporization (2.5×10^6 J kg^{-1}) and the vapour gas constant (461 J kg^{-1} K^{-1}), respectively.

As T_{dew} represents the temperature above which water vapour will achieve saturation under constant water vapour content and pressure, it can be used to measure actual water vapour pressure. RH can thus be deduced by substituting T_{2m} and T_{dew} into equation (1) as $RH = e_{sat}(T_{dew})/e_{sat}(T_{2m})$.

SH refers to the ratio of the water vapour mass to the total air mass, which can be calculated using pr and T_{dew}[53]:

$$SH = 0.622\frac{e_{sat}(T_{dew})}{pr - 0.378e_{sat}(T_{dew})} \quad (2)$$

T_{max}–TWS coupling and impacts

The T_{max}–TWS coupling was evaluated by calculating Pearson's correlation coefficient between them. We also sorted observed T_{max} and daily SM (daily or monthly TWS) from the flux tower sites (GLDAS or GRACE/GRACE-FO) into 10 × 10 percentile bins in each site and calculated the mean probability of each percentile bin of T_{max} and SM (or TWS) across the 73 sites. We calculated mean daily anomalies of GPP, TER and NEP in the 10 × 10 percentile bins to assess the observed mean responses of these variables to daily temperature and TWS (or SM), especially the responses to extreme high T_{max} and low TWS (or SM). The dry extremes were determined according to TWS-DSI ≤ −0.8, and the heat extremes were identified by daily T_{max} being above its 90th percentile over the whole observation period (or the historical period of model simulations). In addition, we examined the impacts of compound extremes on a variety of water and heat variables (for example, RH, SH and CAPE). For both observations and GCM simulations, we calculated their anomalies as the difference between the daily (monthly) values in heat extremes and CDHWs (droughts) and the mean values in the warm season. As the daily carbon flux data are not typically archived for most GCMs, we assessed the responses of GPP, TER and NEP to heat (measured by monthly T_{max} above its 90th percentile over the historical period), droughts and the concurring conditions at a monthly scale, in historical and future simulations individually.

TWS-DSI

The recently proposed TWS-DSI was used to identify terrestrial drought conditions[54]. A negative TWS-DSI means that the TWS is lower than the average level during the study period; this was used to represent drought magnitudes. The TWS-DSI was deduced as follows:

$$TWS - DSI_{i,j} = (TWS_{i,j} - \overline{TWS_j})/\sigma_j \quad (3)$$

where $TWS_{i,j}$ refers to the TWS anomalies at year i and month j, and $\overline{TWS_j}$ and σ_j denote the mean value and standard deviation of TWS anomalies at month j.

For the GCM–THM TWS outputs, we determined the same time-mean baseline as the GRACE/GRACE-FO dataset, and we thus obtained monthly TWS anomalies during 1976–2099 after subtracting the mean values of TWS for 2004–2009. In calculating the mean and standard deviation of TWS for any specified period, we used a common reference period (that is, 1976–2099) to avoid potential exaggeration in estimating TWS variability and drought evolution, and for consistent comparison. The drought pattern in the historical period may differ slightly in each RCP/SSP, as the TWS-DSI is derived from both historical and future TWS data. The droughts are characterized by four metrics: frequency, the total number of drought events during the study period; days, defined as the total number of drought months; the commonly used drought severity (D_s); and duration, identified by the run theory[34]. The probability density functions for both the globe and different Giorgi climate regions during two periods were estimated using the non-parametric kernel density method. To compare the different drought indices, we first fit the monthly ERA5 precipitation and runoff data to the gamma distribution function to obtain monthly climatological distributions. We then converted the cumulative probabilities

to standard normal deviates by inversing the respective cumulative distribution function, and thus the standardized precipitation index and standardized runoff index were calculated. Besides these two indices and the Climatic Research Unit SPEI data, we used both ERA5 and GLEAM SM data instead of TWS to characterize the drought conditions.

CDHW identification

A heatwave refers to a spell of at least three consecutive days with T_{max} exceeding the heat threshold, which is defined as the 90th percentile of T_{max} in the warm season over the entire study period. Considering possible epidemiological significance[55], two successive heatwave events are considered independent if separated by a minimum of two days; otherwise, they are clustered into a single event. We also assessed the heatwave characteristics using four metrics: frequency, days, duration and the heatwave severity (HW_s). HW_s was estimated by summing the daily T_{max} anomalies:

$$HW_s = \sum_{d=1}^{d=D} \left(\frac{T_{max,d} - T_{25p}}{T_{75p} - T_{25p}} \right) \quad ; D \geq 3 \tag{4}$$

where D indicates the duration of the heatwave event, $T_{max,d}$ is the daily maximum temperature at day d in this event, and T_{25p} and T_{75p} are the 25th and 75th percentiles of T_{max} in the warm season, respectively.

CDHWs are identified when a heatwave coincides with a monthly drought event[24]. We also calculated $CDHW_r$ to represent CDHW characteristics on the basis of the ratio of the total number of CDHWs and heatwave events occurring at any given location[24]. The severity of CDHWs was estimated as the product of the daily standardized values of T_{max} and the daily TWS-DSI (the value was determined to be the same with the monthly TWS-DSI for each month) in the CDHW event. The severity for a CDHW ($CDHW_s$) is thus given as:

$$CDHW_s = \sum_{d=1}^{d=CDHW_D} \left[(-1 \times \text{TWS-DSI}_d) \times \left(\frac{T_{max,d} - T_{25p}}{T_{75p} - T_{25p}} \right) \right] \quad ; CDHW_D \geq 3 \tag{5}$$

where $CDHW_D$ represents the duration of the coinciding days, and TWS-DSI_d is the TWS-DSI value at day d, which is consistent at a monthly scale.

Bivariate risk assessments of CDHW

We first quantified changes in the frequency, days, duration and severity (and $CDHW_r$) of droughts, heatwaves and CDHWs from the historical period to the future period (2070–2099). Furthermore, to jointly understand the changes in both heatwave and drought severity under CDHW hazards, we analysed the shifts of the bivariate return period by using non-stationary copulas, which are often used to describe the dependence between physical variables[56]. Here we initially estimated the marginal distributions of HW_s and D_s of CDHWs during the historical period by using six candidate distributions (that is, gamma, normal, GEV, Weibull, log-normal and inverse Gaussian). We then considered commonly used bivariate copula families (Gaussian copula, Student's t copula and Archimedean copulas) to link the marginal distributions of historical HW_s and D_s. To reduce the uncertainty sourced from different marginal and joint distributions, only the best-fitting functions were used for fitting HW_s and D_s under future climates. We chose the Akaike information criterion to determine both the best-fitting marginal distributions and the associated copulas[57], and we employed the 'AND' definition of JRP to measure the bivariate hazards of CDHWs, which is consistent with the approach of counting concurrent exceedances[58]. The JRP is therefore given as:

$$\text{JRP} = \frac{E}{1 - F_{HW} - F_{DR} + C(F_{HW}, F_{DR})} \tag{6}$$

where F_{HW} (F_{DR}) is the marginal cumulative distribution of HW_s (D_s), $C(F_{HW}, F_{DR})$ represents the joint distribution of F_{HW} and F_{DR}, and E denotes the average inter-arrival time between compound events.

Using copulas to model the dependence of heatwave and drought allows an assessment of the change in the likelihood of extreme (that is, 50-year) CDHWs. Therefore, the time-varying copula functions of HW_s and D_s were constructed by moving a 30-year window, with the aim to investigate the shifts of the bivariate CDHW hazard as well as the socio-economic exposure to increasing risks under climate change. We first estimated the quantiles of HW_s and D_s under a given JRP during the historical period (T_h, determined as the 50-year JRP in this study). As there are infinite points on the isoline of a given JRP, the likelihood of each event must be taken into consideration. The most likely realization is therefore optimized by achieving the maximum joint probability density[34,59]:

$$\begin{cases} (HW_s^*, D_s^*) = \arg\max f(\text{HW}, \text{DR}) = c(F_{HW}, F_{DR}) \times f_{HW} \times f_{DR} \\ c(F_{HW}, F_{DR}) = \frac{dC(F_{HW}, F_{DR})}{d(F_{HW})d(F_{DR})} \end{cases} \tag{7}$$

where $c(F_{HW}, F_{DR})$ is the copula probability density function; f_{HW} and f_{DR} denote the probability density functions of F_{HW} and F_{DR}, respectively; and (HW_s^*, D_s^*) is the most likely realization under the given historical JRP (T_h).

After estimating (HW_s^*, D_s^*) during the historical period by linking equations (6) and (7), we used the 30-year period as a sliding time window (consistent with the length of the historical period), and we constructed the time-varying marginal distributions and copula functions moving from 2006 to 2099 at a 30-year window. After substituting (HW_s^*, D_s^*) into the time-varying distribution function of the kth sliding window in the future period (T_f), we calculated an updated JRP, $T_f(k)$. If $T_f(k) < T_h$, it means that the bivariate CDHW risk in the kth time window increases, and vice versa. As a result, the socio-economic exposure arising from increasing bivariate risks can be measured by the following formula:

$$E_{POP} = \frac{I[T_h - T_f(k)] \times POP_k}{\sum_{k=N_1}^{k=N_2} POP_k} \times 100\% \tag{8}$$

$$E_{GDP} = \frac{I[T_h - T_f(k)] \times GDP_k}{\sum_{k=N_1}^{k=N_2} GDP_k} \times 100\% \tag{9}$$

where E_{POP} and E_{GDP} denote the population and GDP exposures to increasing bivariate CDHW risks, respectively; POP_k and GDP_k denote the population and GDP in the kth year; $I(\cdot)$ is an indication function (when $T_h - T_f(k) > 0$, $I = 1$; otherwise, $I = 0$); and N_1 and N_2 denote the starting and ending years of the study period, respectively.

Uncertainty decomposition using MANOVA

To project future changes in the JRP of CDHWs, we implemented 96 scenarios in the impact modelling chain, which consists of three RCPs, four GCMs and eight THMs under ISIMIP2b. In this study, the overall uncertainty was estimated by the variance of the average JRP during the future period and was then decomposed into the contributions from different sources using MANOVA[60]. The change in the climatic indicator $\Delta y_{i,j,k}$ (that is, the updated JRP of the historical 50-year CDHW in this study) is assumed to follow the following model:

$$\Delta y_{i,j,k} = \mu + R_i + G_j + H_k + I_{i,j,k} \tag{10}$$

where μ represents the mean change of the model ensemble of the climatic indicator; R_i, G_j and H_k represent the effects on the climatic indicator of the ith RCP, the jth GCM and the kth THM, respectively; and $I_{i,j,k}$ represents the sum of the effects due to the interactions between different sources.

On the basis of the MANOVA method, the total variance (overall uncertainty, VT) can be decomposed into contributions from different sources as follows:

$$VT = VR + VG + VH + VI_{RG} + VI_{RH} + VI_{RGH} \quad (11)$$

where VR, VG and VH represent the variance contributed by the effects of RCPs, GCMs and THMs, respectively; and VI_{RG}, VI_{RH} and VI_{RGH} represent the variance from interaction effects between RCPs–GCMs, RCPs–THMs and RCPs–GCMs–THMs, respectively. By dividing the variance from different sources by the total variance, we obtained the fractional contributions of different sources to the overall uncertainty. We also employed MANOVA to quantify the contributions of uncertainty sources in the CMIP6-based projections.

Reporting summary

Further information on research design is available in the Nature Portfolio Reporting Summary linked to this article.

Data availability

The CMIP5-based TWS simulations are freely available from the ISIMIP project portal (https://data.isimip.org/search/tree/ISIMIP2b/InputData/climate/). The three GRACE/GRACE-FO products are available from http://www2.csr.utexas.edu/grace/, https://grace.jpl.nasa.gov/data/get-data/ and https://earth.gsfc.nasa.gov. The long-term reconstructed TWS data are available on Figshare (https://doi.org/10.6084/m9.figshare.7670849). The TWS simulations under CMIP6 are available at the repository in the Open Science Framework (https://osf.io/hy96r/); this dataset cannot be accessed now, because the data are in an embargo period and currently shared only among the ISIMIP participants. The SPEI dataset is available at https://spei.csic.es/database.html. The GLDAS-2.2 data are available at https://ldas.gsfc.nasa.gov/gldas/forcing-data. The ERA5 reanalysis data are from https://www.ecmwf.int/en/forecasts/datasets/reanalysis-datasets/era5. The GLEAM 3.5a data are from https://www.gleam.eu/. The FLUXNET2015 dataset is from https://fluxnet.org/data/fluxnet2015-dataset/. The gridded SIF dataset is from https://doi.org/10.17605/OSF.IO/8XQY6, and the gridded GPP dataset is available from https://data.tpdc.ac.cn/en/data/582663f5-3be7-4f26-bc45-b56a3c4fc3b7/. The global gridded population data are available from https://sedac.ciesin.columbia.edu/data/set/gpw-v4-population-density-adjusted-to-2015-unwpp-country-totals-rev11; the global gridded GDP data and the GDP per capita data are available from https://datadryad.org/stash/dataset/doi:10.5061/dryad.dk1j0. The BEST dataset is available at Berkeley Earth (http://berkeleyearth.org/data/).

Code availability

The R (version 4.1.0) code used for producing Figs. 1–5 and the MATLAB (version 2020a) code used for data analysis are available at the repository in the Open Science Framework (https://osf.io/dnuxv/).

References

1. Zhang, P. et al. Abrupt shift to hotter and drier climate over inner East Asia beyond the tipping point. *Science* **370**, 1095–1099 (2020).
2. Jaeger, W. K. et al. Scope and limitations of drought management within complex human–natural systems. *Nat. Sustain.* **2**, 710–717 (2019).
3. Lim, E. P. et al. Australian hot and dry extremes induced by weakenings of the stratospheric polar vortex. *Nat. Geosci.* **12**, 896–901 (2019).
4. Bevacqua, E. et al. Precipitation trends determine future occurrences of compound hot–dry events. *Nat. Clim. Change* **12**, 350–355 (2022).
5. Dirmeyer, P. A., Jin, Y., Singh, B. & Yan, X. Evolving land–atmosphere interactions over North America from CMIP5 simulations. *J. Clim.* **26**, 7313–7327 (2013).
6. Alizadeh, M. R. et al. A century of observations reveals increasing likelihood of continental-scale compound dry–hot extremes. *Sci. Adv.* **6**, eaaz4571 (2020).
7. Reichstein, M. et al. Climate extremes and the carbon cycle. *Nature* **500**, 287–295 (2013).
8. Gampe, D. et al. Increasing impact of warm droughts on northern ecosystem productivity over recent decades. *Nat. Clim. Change* **11**, 772–779 (2021).
9. Williams, A. P. et al. Temperature as a potent driver of regional forest drought stress and tree mortality. *Nat. Clim. Change* **3**, 292–297 (2013).
10. Anderegg, W. R. et al. Pervasive drought legacies in forest ecosystems and their implications for carbon cycle models. *Science* **349**, 528–532 (2015).
11. Zampieri, M., Ceglar, A., Dentener, F. & Toreti, A. Wheat yield loss attributable to heat waves, drought and water excess at the global, national and subnational scales. *Environ. Res. Lett.* **12**, 064008 (2017).
12. Guerreiro, S. B. et al. Future heat-waves, droughts and floods in 571 European cities. *Environ. Res. Lett.* **13**, 034009 (2018).
13. Keenan, T. F. et al. A constraint on historic growth in global photosynthesis due to increasing CO_2. *Nature* **600**, 253–258 (2021).
14. Noon, M. L. et al. Mapping the irrecoverable carbon in Earth's ecosystems. *Nat. Sustain.* **5**, 37–46 (2022).
15. Ciais, P. et al. Europe-wide reduction in primary productivity caused by the heat and drought in 2003. *Nature* **437**, 529–533 (2005).
16. Ruehr, N. K., Grote, R., Mayr, S. & Arneth, A. Beyond the extreme: recovery of carbon and water relations in woody plants following heat and drought stress. *Tree Physiol.* **39**, 1285–1299 (2019).
17. Lobell, D. B., Deines, J. M. & Tommaso, S. D. Changes in the drought sensitivity of US maize yields. *Nat. Food* **1**, 729–735 (2020).
18. Schwalm, C. R. et al. Global patterns of drought recovery. *Nature* **548**, 202–205 (2017).
19. Zhou, S., Zhang, Y., Williams, A. P. & Gentine, P. Projected increases in intensity, frequency, and terrestrial carbon costs of compound drought and aridity events. *Sci. Adv.* **5**, eaau5740 (2019).
20. Mazdiyasni, O. & AghaKouchak, A. Substantial increase in concurrent droughts and heatwaves in the United States. *Proc. Natl Acad. Sci. USA* **112**, 11484–11489 (2015).
21. Zscheischler, J. et al. A typology of compound weather and climate events. *Nat. Rev. Earth Environ.* **1**, 333–347 (2020).
22. Naumann, G. et al. Increased economic drought impacts in Europe with anthropogenic warming. *Nat. Clim. Change* **11**, 485–491 (2021).
23. Satoh, Y. et al. A quantitative evaluation of the issue of drought definition: a source of disagreement in future drought assessments. *Environ. Res. Lett.* **16**, 104001 (2021).
24. Mukherjee, S. & Mishra, A. K. Increase in compound drought and heatwaves in a warming world. *Geophys. Res. Lett.* **48**, e2020GL090617 (2021).
25. Zhao, M. et al. Ecological restoration impact on total terrestrial water storage. *Nat. Sustain.* **4**, 56–62 (2021).
26. Pokhrel, Y. et al. Global terrestrial water storage and drought severity under climate change. *Nat. Clim. Change* **11**, 226–233 (2021).
27. Zhang, Y., Joiner, J., Alemohammad, S. H., Zhou, S. & Gentine, P. A global spatially contiguous solar-induced fluorescence (CSIF) dataset using neural networks. *Biogeosci* **15**, 5779–5800 (2018).

28. Zhang, Y. et al. A global moderate resolution dataset of gross primary production of vegetation for 2000–2016. *Sci. Data* **4**, 170165 (2017).
29. Zhou, S. et al. Land–atmosphere feedbacks exacerbate concurrent soil drought and atmospheric aridity. *Proc. Natl Acad. Sci. USA* **116**, 18848–18853 (2019).
30. Lobell, D. B. et al. The critical role of extreme heat for maize production in the United States. *Nat. Clim. Change* **3**, 497–501 (2013).
31. Drake, J. E. et al. A common thermal niche among geographically diverse populations of the widely distributed tree species *Eucalyptus tereticornis*: no evidence for adaptation to climate-of-origin. *Glob. Change Biol.* **23**, 5069–5082 (2017).
32. Novick, K. A. et al. The increasing importance of atmospheric demand for ecosystem water and carbon fluxes. *Nat. Clim. Change* **6**, 1023–1027 (2016).
33. Nemani, R. R. et al. Climate-driven increases in global terrestrial net primary production from 1982 to 1999. *Science* **300**, 1560–1563 (2003).
34. Yin, J. et al. Projection of droughts and their socioeconomic exposures based on terrestrial water storage anomaly over China. *Sci. China Earth Sci.* **65**, 1772–1787 (2022).
35. Campbell, J. E. et al. Large historical growth in global terrestrial gross primary production. *Nature* **544**, 84–87 (2017).
36. Wang, X. et al. Emergent constraint on crop yield response to warmer temperature from field experiments. *Nat. Sustain.* **3**, 908–916 (2020).
37. Allen, C. D., Breshears, D. D. & McDowell, N. G. On underestimation of global vulnerability to tree mortality and forest die-off from hotter drought in the Anthropocene. *Ecosphere* **6**, 129 (2015).
38. Rodrigues, R. R. & Woollings, T. Impact of atmospheric blocking on South America in austral summer. *J. Clim.* **30**, 1821–1837 (2017).
39. Büntgen, U. et al. Recent European drought extremes beyond Common Era background variability. *Nat. Geosci.* **14**, 190–196 (2021).
40. Schumacher, D. L. et al. Amplification of mega-heatwaves through heat torrents fuelled by upwind drought. *Nat. Geosci.* **12**, 712–717 (2019).
41. Hallegatte, S. et al. Poverty and climate change: introduction. *Environ. Dev. Econ.* **23**, 217–233 (2018).
42. Fankhauser, S. & McDermott, T. K. J. Understanding the adaptation deficit: why are poor countries more vulnerable to climate events than rich countries? *Glob. Environ. Change* **27**, 9–18 (2014).
43. Burke, M., Hsiang, S. & Miguel, E. Global non-linear effect of temperature on economic production. *Nature* **527**, 235–239 (2015).
44. Elkouk, A. et al. Implications of changes in climate and human development on 21st-century global drought risk. *J. Environ. Manage.* **317**, 115378 (2022).
45. Lange, S. Bias correction of surface downwelling longwave and shortwave radiation for the EWEMBI dataset. *Earth Syst. Dyn.* **9**, 627–645 (2018).
46. Lange, S. Trend-preserving bias adjustment and statistical downscaling with ISIMIP3BASD (v1. 0). *Geosci. Model Dev.* **12**, 3055–3070 (2019).
47. Humphrey, V. & Gudmundsson, L. GRACE-REC: a reconstruction of climate-driven water storage changes over the last century. *Earth Syst. Sci. Data* **11**, 1153–1170 (2019).
48. Reichstein, M. et al. On the separation of net ecosystem exchange into assimilation and ecosystem respiration: review and improved algorithm. *Glob. Change Biol.* **11**, 1424–1439 (2005).
49. Pastorello, G. et al. The FLUXNET2015 dataset and the ONEFlux processing pipeline for eddy covariance data. *Sci. Data* **7**, 225 (2020).
50. Kummu, M. et al. Gridded global datasets for gross domestic product and Human Development Index over 1990–2015. *Sci. Data* **5**, 180004 (2018).
51. Jing, C. et al. Population, urbanization and economic scenarios over the Belt and Road region under the Shared Socioeconomic Pathways. *J. Geogr. Sci.* **30**, 68–84 (2020).
52. Koutsoyiannis, D. Clausius–Clapeyron equation and saturation vapor pressure: simple theory reconciled with practice. *Eur. J. Phys.* **33**, 295–305 (2012).
53. Simmons, A. J., Untch, A., Jakob, C., Kallberg, P. & Unden, P. Stratospheric water vapor and tropical tropopause temperatures in ECMWF analyses and multi-year simulations. *Q. J. R. Meteorol. Soc.* **125**, 353–386 (1999).
54. Zhao, M., Velicogna, I. & Kimball, J. S. Satellite observations of regional drought severity in the continental United States using GRACE-based terrestrial water storage changes. *J. Clim.* **30**, 6297–6308 (2017).
55. Keellings, D. & Waylen, P. Increased risk of heat waves in Florida: characterizing changes in bivariate heat wave risk using extreme value analysis. *Appl. Geogr.* **46**, 90–97 (2014).
56. Yin, J. et al. Global increases in lethal compound heat stress: hydrological drought hazards under climate change. *Geophys. Res. Lett.* **49**, e2022GL100880 (2022).
57. Akaike, H. A new look at the statistical model identification. *IEEE Trans. Autom. Contr.* **19**, 716–723 (1974).
58. Zscheischler, J. & Seneviratne, S. I. Dependence of drivers affects risks associated with compound events. *Sci. Adv.* **3**, e1700263 (2017).
59. Salvadori, G. et al. A multivariate copula-based framework for dealing with hazard scenarios and failure probabilities. *Water Resour. Res.* **52**, 3701–3721 (2016).
60. Chegwidden, O. S. et al. How do modeling decisions affect the spread among hydrologic climate change projections? Exploring a large ensemble of simulations across a diversity of hydroclimates. *Earth's Future* **7**, 623–637 (2019).

Acknowledgements

J.Y. acknowledges support from the National Natural Science Foundation of China (grant no. 52009091). L.S. acknowledges support from UK Research and Innovation (grant no. MR/V022008/1). Y.P. acknowledges support from the National Science Foundation (CAREER Award, grant no. 1752729). J.Y. is also supported by the Fundamental Research Funds for the Central Universities (grant no. 2042022kf1221). The numerical calculations in this paper were performed on the supercomputing system in the Supercomputing Center of Wuhan University.

Author contributions

J.Y. conceived and designed the study. J.Y. processed the model simulations and reanalysis data. N.H. conducted the H08 simulations. J.Y., P.G., L.S., L.G., Y.P., S.G., L.X. and W.S. contributed to the data analysis and interpretation. J.Y. drafted the manuscript. All authors edited the manuscript.

Competing interests

The authors declare no competing interests.

Additional information

Extended data is available for this paper at https://doi.org/10.1038/s41893-022-01024-1.

Supplementary information The online version contains supplementary material available at https://doi.org/10.1038/s41893-022-01024-1.

Correspondence and requests for materials should be addressed to Jiabo Yin.

Peer review information *Nature Sustainability* thanks William Jaeger and Sourav Mukherjee for their contribution to the peer review of this work.

https://doi.org/10.1038/s41893-022-01024-1

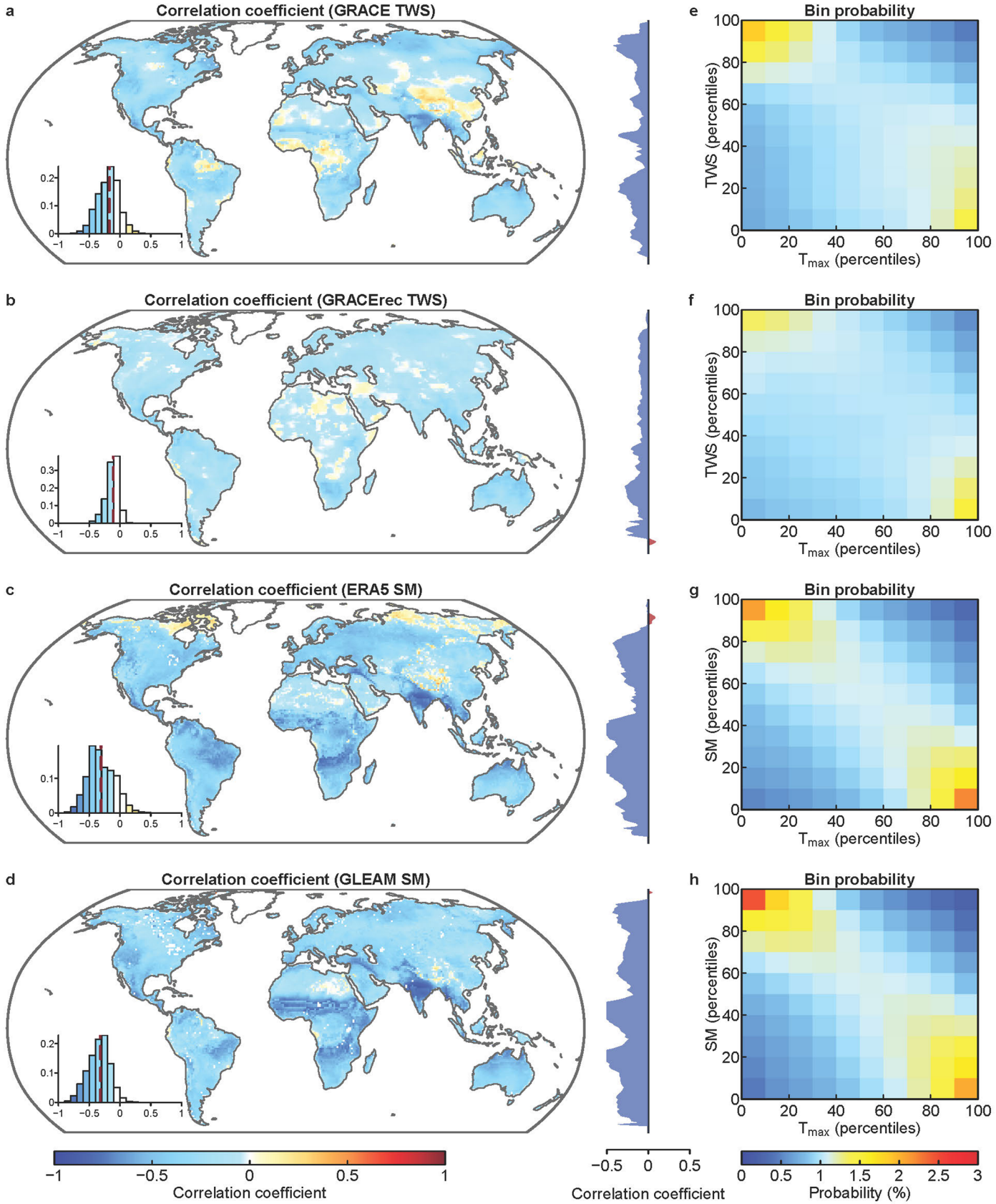

Extended Data Fig. 1 | Relationship between daily maximum near-surface temperature (T_{max}) and terrestrial water storage (TWS) or root-zone soil moisture (SM) during 2002–2020. a-d, Pearson's correlation coefficient between: monthly GRACE/GRACE-FO ensemble mean TWS and ERA5 T_{max} (**a**), monthly reconstructed TWS and T_{max} from Berkeley Earth Surface Temperatures (**b**), daily ERA5 SM and T_{max} (**c**), daily GLEAM SM and ERA5 T_{max} (**d**). Insets in **a-d** show the histogram of the correlation coefficient, with the dashed vertical line representing the median value. The graph on the right of each panel shows the latitudinal median. **e-h**, Mean probability of each percentile bin across all land grid cells (excluding Greenland and Antarctica in all analyses).

https://doi.org/10.1038/s41893-022-01024-1

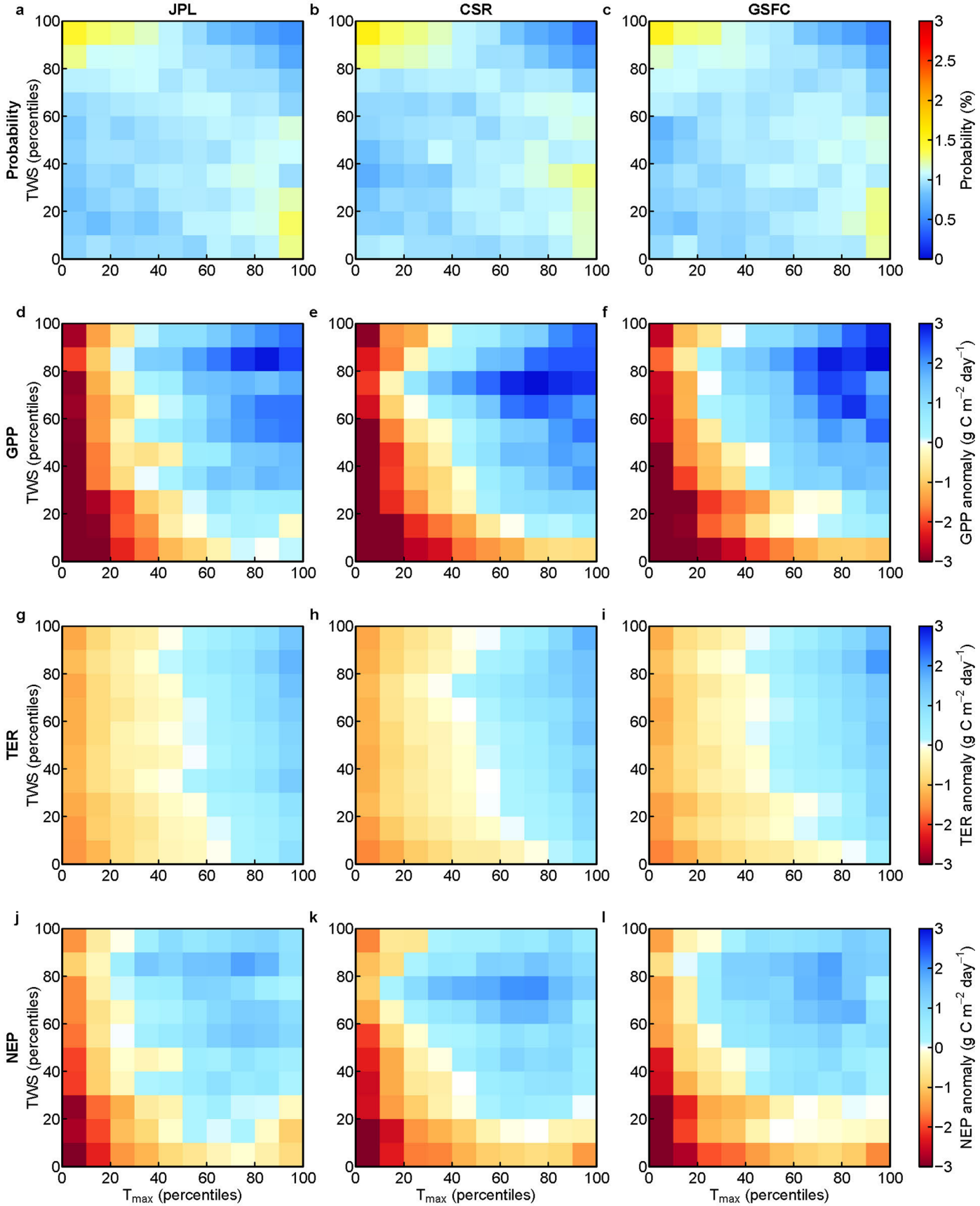

Extended Data Fig. 2 | See next page for caption.

https://doi.org/10.1038/s41893-022-01024-1

Extended Data Fig. 2 | Coupling of T_{max} and monthly TWS from the three GRACE/GRACE-FO solutions dataset and their impacts on terrestrial carbon uptake. a-c, Probability of each percentile bin of T_{max} and monthly TWS across 73 flux tower sites. **d-f**, Mean anomalies of GPP for each percentile bin of T_{max} and TWS. **g-i**, Mean anomalies of TER for each percentile bin of T_{max} and TWS. **j-l**, Mean anomalies of NEP for each percentile bin of T_{max} and TWS. The three columns represent the GRACE/GRACE-FO TWS data produced from JPL, CSR and GSFC, respectively. At each site, anomalies of GPP, TER, and NEP are calculated as the difference between the daily values in extreme events and the mean daily values in the warm season (defined as days when running 7-day mean temperatures are higher than the 60^{th} percentile of daily temperature for the site).

https://doi.org/10.1038/s41893-022-01024-1

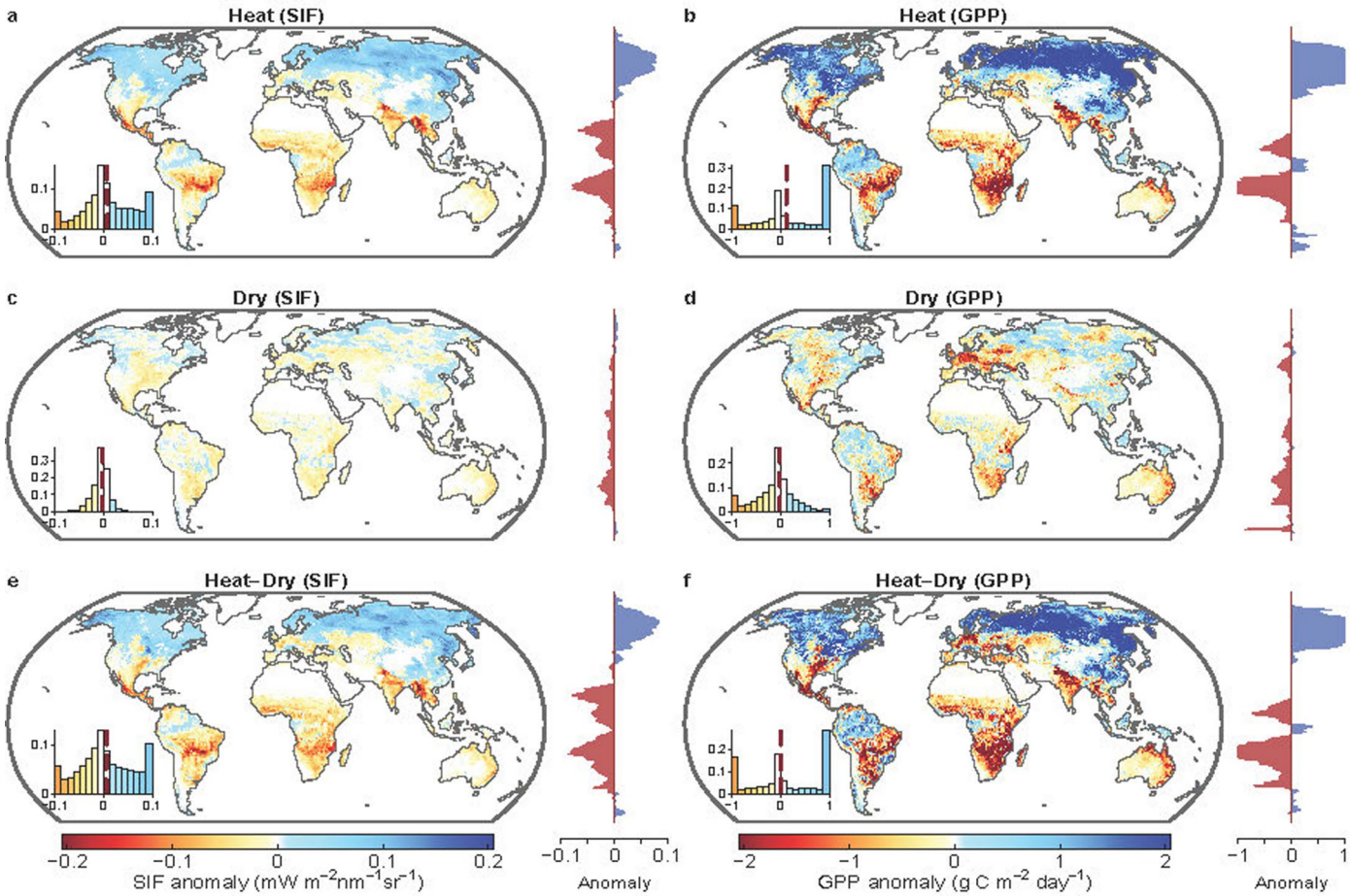

Extended Data Fig. 3 | Anomalies of SIF and GPP during extreme climatic events. a, **b**, Anomalies of SIF (**a**) and GPP (**b**) during extreme heat events. **c**-**d**, Anomalies of SIF (**c**) and GPP (**d**) during extreme dry events. **e**, **f**, Anomalies of SIF (**e**) and GPP (**f**) in concurrent heat and dry conditions. At each grid, anomalies of SIF (GPP) are calculated as the difference between the 4-day (8-day) values in extreme events and the mean 4-day (8-day) values in the warm season. Dry conditions are identified using GRACE/GRACE-FO ensemble mean TWS data, and the heat conditions are identified by ERA5 T_{max}. Insets show the histogram of the anomalies, with the dashed vertical line representing the median value. The graph on the right shows the latitudinal median value.

https://doi.org/10.1038/s41893-022-01024-1

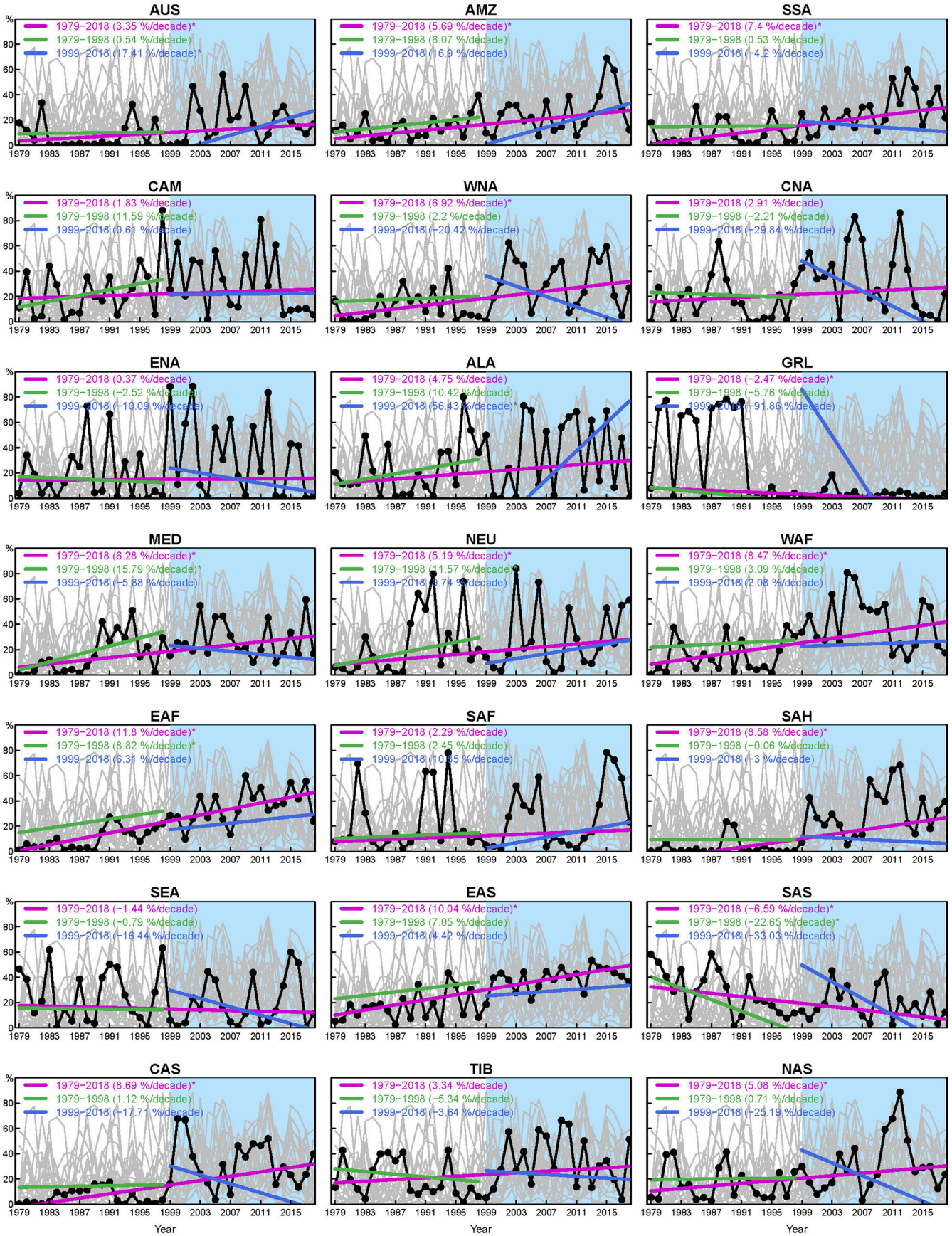

Extended Data Fig. 4 | Temporal dynamics of the GDP exposures to CDHW in 21 Giorgi climate regions. Each panel has a cluster of 21 grey lines, which show the ensemble of the regional GDP exposures in all regions. The black line in each figure represents the exposure value in each region, and the color lines represent trends of GDP exposures during recent, past and entire periods. The droughts are identified by reconstructed TWS data, and the heatwaves are detected by using T_{max} from the BEST dataset. The * indicates the trend is significant ($p < 0.05$) detected by Mann-Kendall test.

https://doi.org/10.1038/s41893-022-01024-1

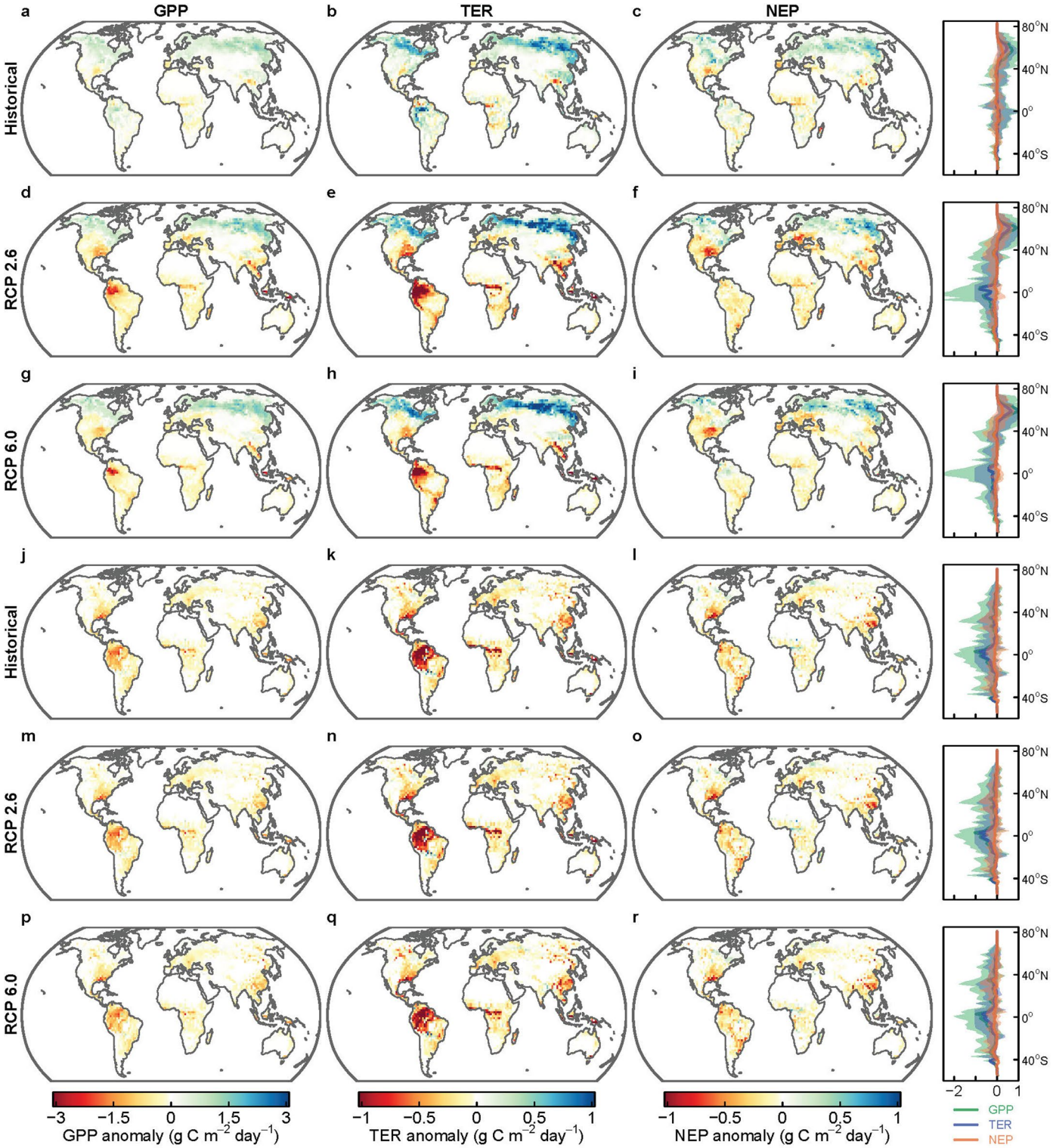

Extended Data Fig. 5 | Anomalies of GPP, TER and NEP due to extreme heat or drought conditions in the GFDL-CLM4.5 model. a-i, Anomalies of carbon fluxes in the historical period (**a-c**), RCP 2.6 (**d-f**) and RCP 6.0 (**g-i**) due to extreme heat conditions (monthly T_{max} above the 90th percentile). **j-r**, Anomalies of carbon fluxes in the historical period (**j-l**), RCP2.6 (**m-o**) and RCP6.0 (**p-r**) due to droughts (TWS-DSI < −0.8). The graph on the right shows the latitudinal median and 90% confidence interval. The TWS and carbon fluxes are projected by CLM4.5 model with bias-corrected GFDL-GCM2M outputs.

https://doi.org/10.1038/s41893-022-01024-1

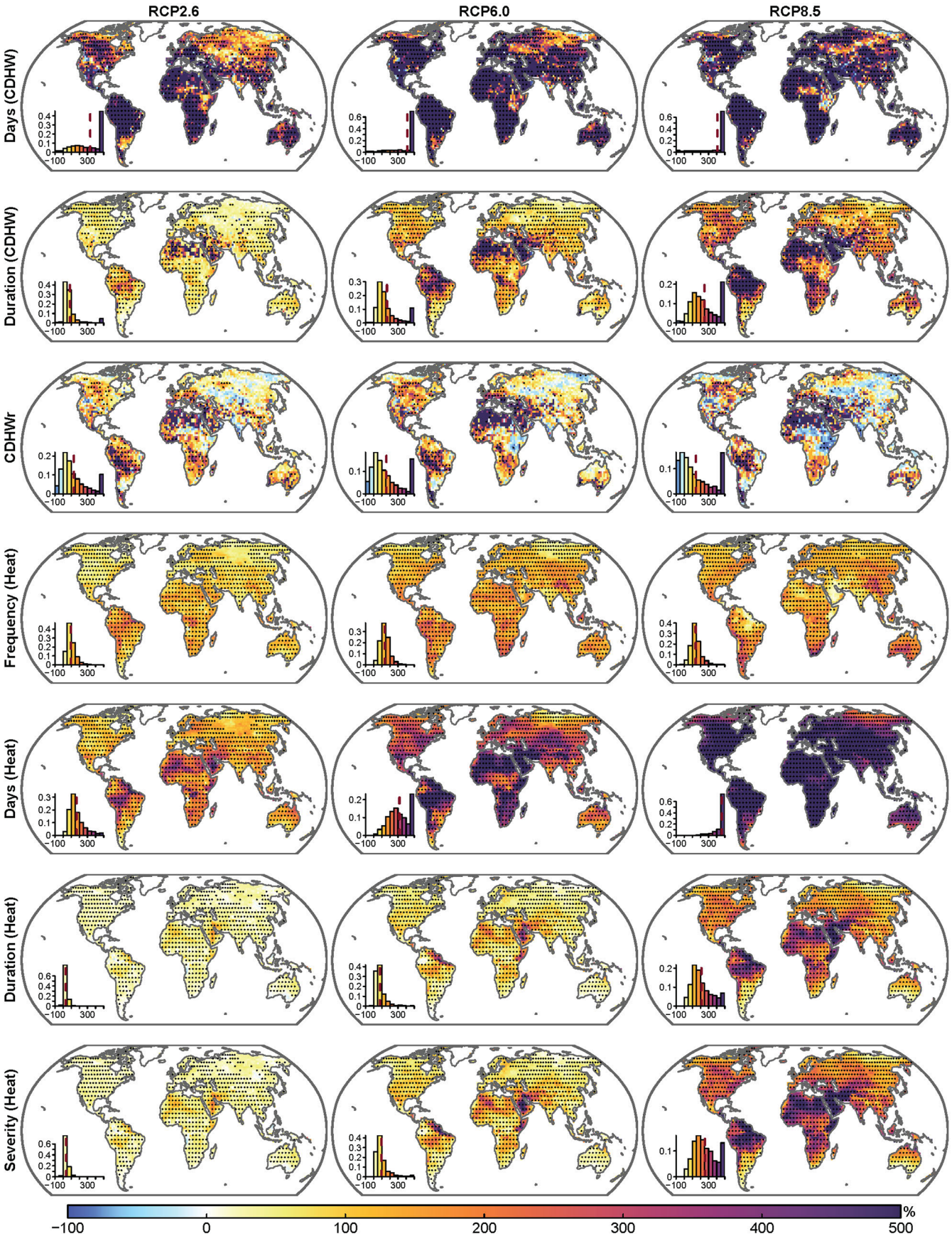

Extended Data Fig. 6 | Future changes in characteristics of CDHW and heatwaves. Insets in each figure show the histogram of the relative change percentages, with the dashed vertical line representing the mean value. Stippling denotes regions where the sign of the relative changes is consistent with the sign of the multi-model means (as shown in the figure) in at least 80% of GCM-THM models. These results are derived from the ISIMIP2b multiple impacts model ensemble.

https://doi.org/10.1038/s41893-022-01024-1

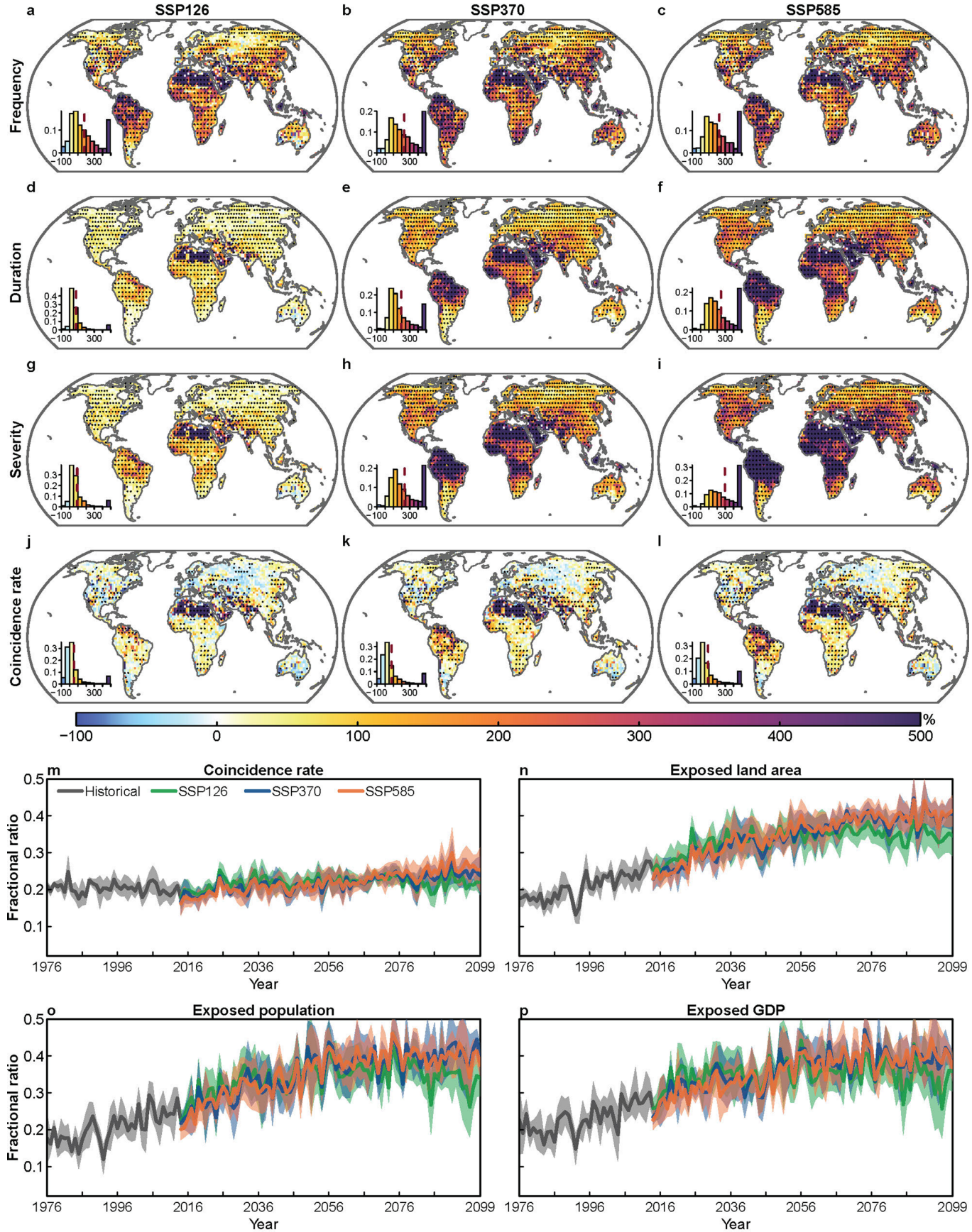

Extended Data Fig. 7 | See next page for caption.

https://doi.org/10.1038/s41893-022-01024-1

Extended Data Fig. 7 | Future changes in the characteristics of CDHW and socioeconomic exposure to CDHW under CMIP6. a-l, Relative changes in the frequency (**a-c**), average duration (**d-f**), average severity (**g-i**) and coincidence rate (**j-l**) of CDHW from the historical to the future periods. **m-p**, Temporal dynamics of the global average coincidence rate (**m**), exposed land area (**n**), exposed population (**o**) and exposed GDP (**p**). Insets in **a-l** show the histogram of the relative change percentages, with the dashed vertical line representing the mean value. Stippling in **a-l** denotes regions where the sign of the relative changes is consistent with the sign of the multi-model means (as shown in the figure) in at least 80% of GCMs. In **m-p**, the shading represents ±1 standard deviation, and only the historical exposures linking to SSP126 TWS data are presented. For projecting CDHW, the TWS is simulated by driving H08 forced by five bias-corrected GCMs under CMIP6.

https://doi.org/10.1038/s41893-022-01024-1

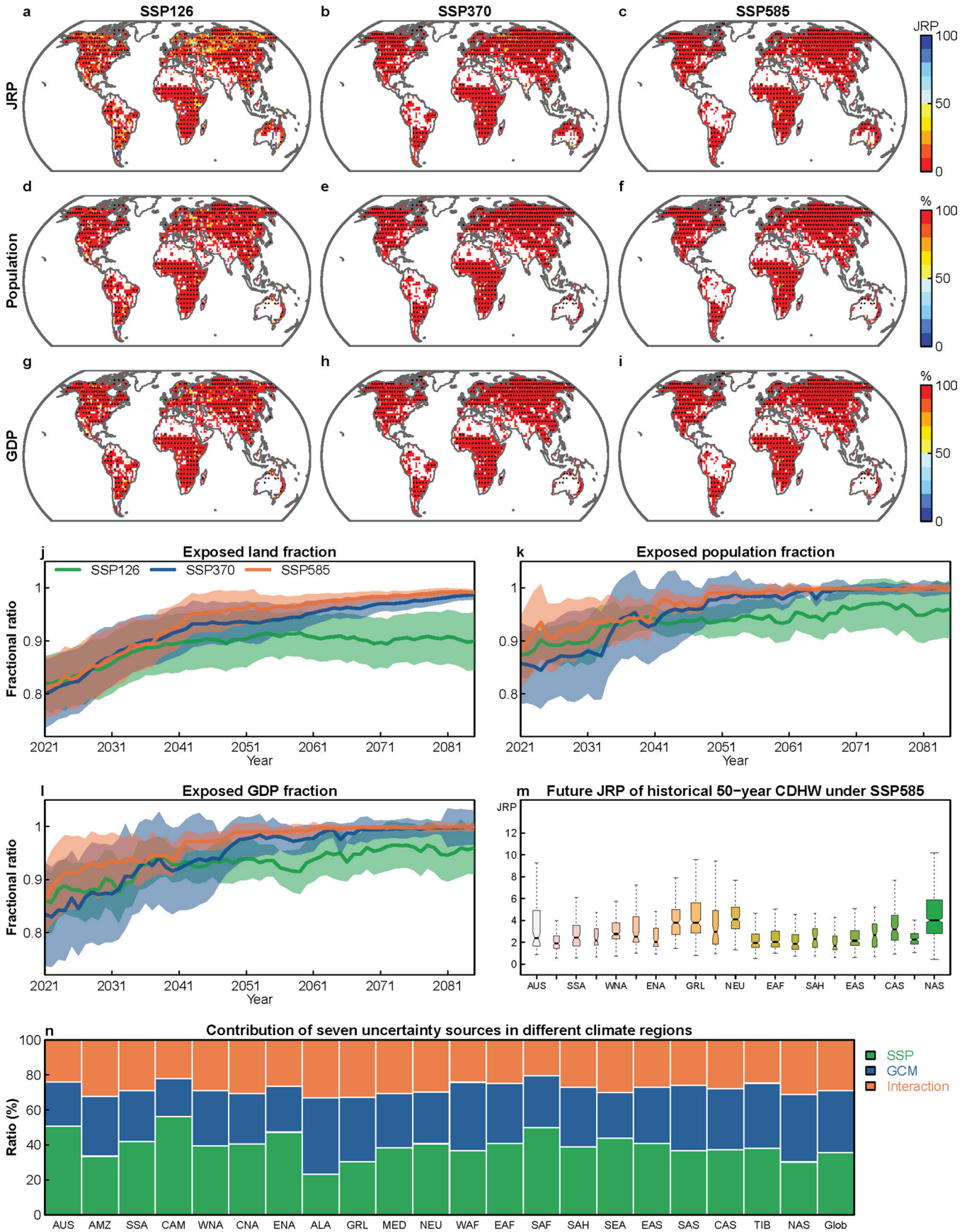

Extended Data Fig. 8 | See next page for caption.

https://doi.org/10.1038/s41893-022-01024-1

Extended Data Fig. 8 | Projected JRP of historical 50-year bivariate CDHW and socioeconomic exposure under CMIP6. a-c, Average JRP in the future period under a non-stationary bivariate framework. **d-i**, Population (**d-f**) and GDP (**g-i**) exposure due to increasing risk of bivariate CDHW in the future period. j-l, Temporal dynamics of the global average exposed land area (**j**), population (**k**) and GDP (**l**) due to increasing CDHW risk; the solid curve and shading indicate multi-model mean ± SD. **m**, Boxplot of updated JRP of the historical 50-year CDHW in different Giorgi climate regions under SSP585; the centre line indicates median value, and the box bounds (whiskers) indicate 25th/75th percentile (min/max) values. **n**, Average contribution ratios of seven uncertainty sources in different Giorgi climate regions and in the global landmass (Glob). Stippling in **a-i** denotes regions where the sign of the JRP is consistent with the sign of the multi-model means (as shown in the figure) in at least 80% of GCMs. For projecting CDHW, the TWS is simulated by driving H08 forced by five bias-corrected GCMs under CMIP6.

https://doi.org/10.1038/s41893-022-01024-1

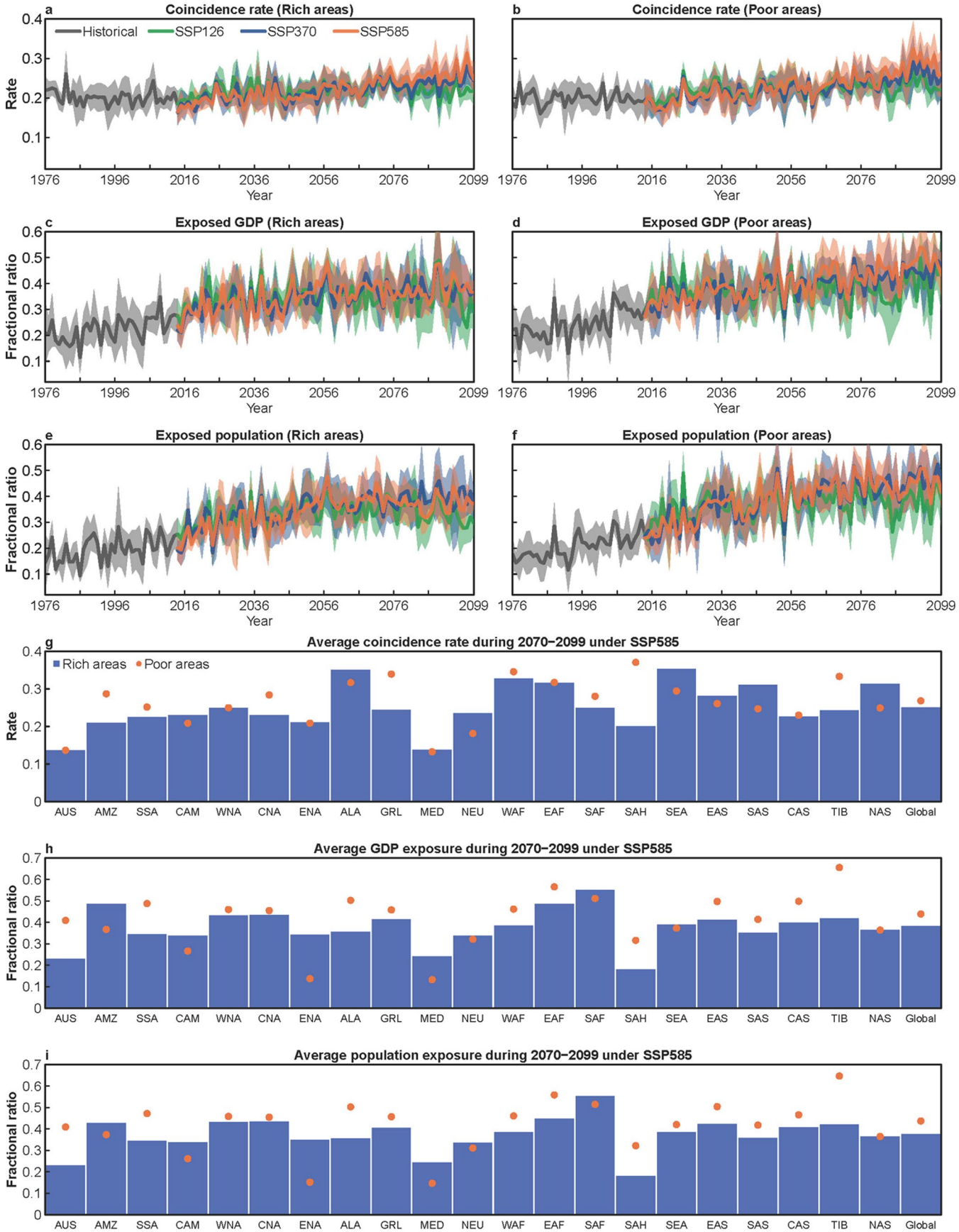

Extended Data Fig. 9 | See next page for caption.

https://doi.org/10.1038/s41893-022-01024-1

Extended Data Fig. 9 | CDHW coincidence rate and socioeconomic exposures to CDHW in rich versus poor areas. a-f, Temporal dynamics of the global average coincidence rate (**a**, **b**), and exposed GDP fraction (**c**, **d**) and population fraction (**e**, **f**) to CDHW. **g-i**, Average coincidence rate (**g**), GDP exposure fraction (**h**) and population exposure fraction (**i**) during 2070–2099 in different Giorgi climate regions under SSP585. In **a-f**, the shading represents ±1 standard deviation, and only the historical exposures linking to SSP126 TWS data are presented. For projecting CDHW, the TWS is simulated by driving H08 forced by five bias-corrected GCMs under CMIP6. Rich (poor) areas are identified where the 2015-year GDP per capita exceeds (is below) the 80th (20th) percentile values in different regions.

https://doi.org/10.1038/s41893-022-01024-1

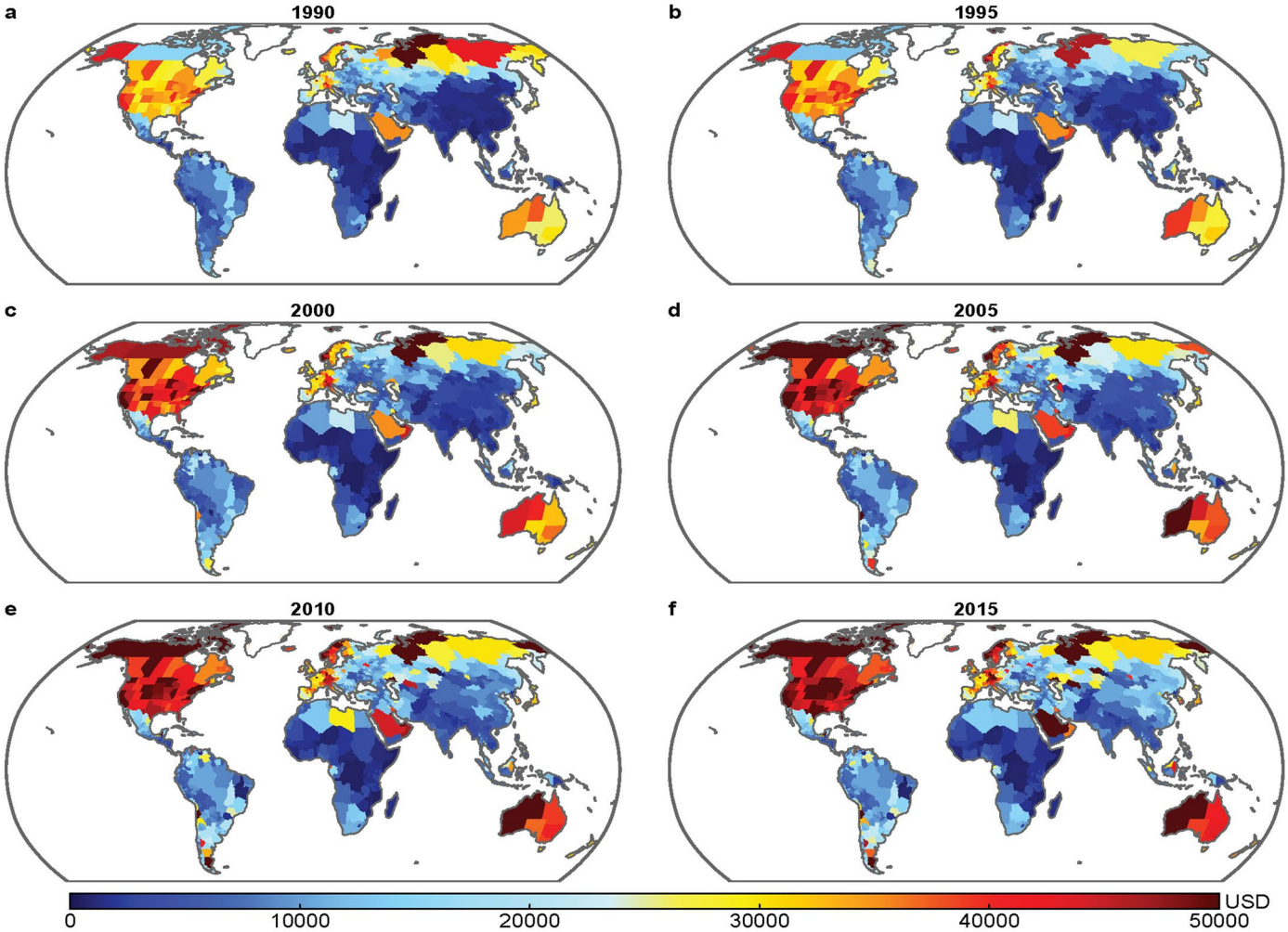

Extended Data Fig. 10 | Gridded Gross Domestic Product (GDP) per capita (purchasing power parity) in constant 2011 international US dollars (USD) for six typical years during 1990–2015. a-f, GDP per capita in year of 1990 (**a**), 1995 (**b**), 2000 (**c**), 2005 (**d**), 2010 (**e**) and 2015 (**f**).

nature portfolio

Corresponding author(s): Jiabo Yin

Last updated by author(s): Nov 4, 2022

Reporting Summary

Nature Portfolio wishes to improve the reproducibility of the work that we publish. This form provides structure for consistency and transparency in reporting. For further information on Nature Portfolio policies, see our Editorial Policies and the Editorial Policy Checklist.

Statistics

For all statistical analyses, confirm that the following items are present in the figure legend, table legend, main text, or Methods section.

n/a	Confirmed
☐	☒ The exact sample size (*n*) for each experimental group/condition, given as a discrete number and unit of measurement
☒	☐ A statement on whether measurements were taken from distinct samples or whether the same sample was measured repeatedly
☐	☒ The statistical test(s) used AND whether they are one- or two-sided *Only common tests should be described solely by name; describe more complex techniques in the Methods section.*
☐	☒ A description of all covariates tested
☒	☐ A description of any assumptions or corrections, such as tests of normality and adjustment for multiple comparisons
☐	☒ A full description of the statistical parameters including central tendency (e.g. means) or other basic estimates (e.g. regression coefficient) AND variation (e.g. standard deviation) or associated estimates of uncertainty (e.g. confidence intervals)
☐	☒ For null hypothesis testing, the test statistic (e.g. *F*, *t*, *r*) with confidence intervals, effect sizes, degrees of freedom and *P* value noted *Give P values as exact values whenever suitable.*
☒	☐ For Bayesian analysis, information on the choice of priors and Markov chain Monte Carlo settings
☒	☐ For hierarchical and complex designs, identification of the appropriate level for tests and full reporting of outcomes
☐	☒ Estimates of effect sizes (e.g. Cohen's *d*, Pearson's *r*), indicating how they were calculated

Our web collection on statistics for biologists contains articles on many of the points above.

Software and code

Policy information about availability of computer code

Data collection	We use the python code released by European Centre for Medium-Range Weather Forecasts to download the ERA5 dataset. For all the other data such as GRACE/GRACE-FO and FLUXNET2015 dataset, we download them in the website without any software.
Data analysis	We use Matlab (version 2020a) and R (version 4.1.0) for data analysis.

For manuscripts utilizing custom algorithms or software that are central to the research but not yet described in published literature, software must be made available to editors and reviewers. We strongly encourage code deposition in a community repository (e.g. GitHub). See the Nature Portfolio guidelines for submitting code & software for further information.

Data

Policy information about availability of data

All manuscripts must include a data availability statement. This statement should provide the following information, where applicable:

- Accession codes, unique identifiers, or web links for publicly available datasets
- A description of any restrictions on data availability
- For clinical datasets or third party data, please ensure that the statement adheres to our policy

The CMIP5-based TWS simulations are freely available from the ISIMIP project portal (https://data.isimip.org/search/tree/ISIMIP2b/InputData/climate/). The three GRACE/GRACE-FO products are available from http://www2.csr.utexas.edu/grace/, https://grace.jpl.nasa.gov/data/get-data/ and https://earth.gsfc.nasa.gov. The long-term reconstructed TWS data are available on Figshare (https://doi.org/10.6084/m9.figshare.7670849). The TWS simulations under CMIP6 are available at the

repository in the Open Science Framework (https://osf.io/hy96r/); this dataset cannot be accessed now, because the data is in embargo period and currently only shared among the ISIMIP participants. The SPEI dataset is available at https://spei.csic.es/database.html. The GLDAS-2.2 data are available at https://ldas.gsfc.nasa.gov/gldas/forcing-data. The ERA5 reanalysis data are from https://www.ecmwf.int/en/forecasts/datasets/reanalysis-datasets/era5. The GLEAM 3.5a data are from https://www.gleam.eu/. The FLUXNET2015 dataset is from https://fluxnet.org/data/fluxnet2015-dataset/. The gridded SIF dataset is from https://doi.org/10.17605/OSF.IO/8XQY6, and the gridded GPP dataset is available from https://data.tpdc.ac.cn/en/data/582663f5-3be7-4f26-bc45-b56a3c4fc3b7/. The global gridded population data are available from https://sedac.ciesin.columbia.edu/data/set/gpw-v4-population-density-adjusted-to-2015-unwpp-country-totals-rev11; the global gridded GDP data and the GDP per capita data are available from https://datadryad.org/stash/dataset/doi:10.5061/dryad.dk1j0. The Berkeley Earth Surface Temperatures (BEST) dataset are available at Berkeley Earth (http://berkeleyearth.org/data/).

Human research participants

Policy information about studies involving human research participants and Sex and Gender in Research.

Reporting on sex and gender	Our study is not relevant with human characteristics such as sex and gender.
Population characteristics	Our study is not relevant with population characteristics.
Recruitment	We do not have human participants in this work.
Ethics oversight	Our study is not relevant with this issue.

Note that full information on the approval of the study protocol must also be provided in the manuscript.

Field-specific reporting

Please select the one below that is the best fit for your research. If you are not sure, read the appropriate sections before making your selection.

☐ Life sciences ☐ Behavioural & social sciences ☒ Ecological, evolutionary & environmental sciences

For a reference copy of the document with all sections, see nature.com/documents/nr-reporting-summary-flat.pdf

Ecological, evolutionary & environmental sciences study design

All studies must disclose on these points even when the disclosure is negative.

Study description	We investigate the physical mechanisms behind compound drought-heatwave events and their impacts on socio-ecosystem productivity. To achieve this goal, we combine satellite observations, reanalysis and model simulations. The data of field measurements are collected from FLUXNET2015, which is also an open access dataset.
Research sample	Our data are collected from international community, such as GRACE/GRACE-FO, ERA5 reanalysis and CMIP6. All the dataset can be access by the public.
Sampling strategy	Our study is conducted at a global scale. We use Person's test to validate the correlation between different variables, and use the M-K method to test the trends.
Data collection	We use the python code released by European Centre for Medium-Range Weather Forecasts to download the ERA5 dataset. For all the other data such as GRACE/GRACE-FO and FLUXNET2015 dataset, we download them in the website without any software.
Timing and spatial scale	Most of our daily data in observational period (1979-2020) have the spatial resolution of 0.25°, and our data of model simulations have the spatial resolution of 0.5°. We conduct our analysis at a global scale.
Data exclusions	We exclude some stations of the FLUXNET2015, because those stations have short observation period. We also provide the lists of our used stations in Supplementary Information.
Reproducibility	All of our results can be repeated by running our codes.
Randomization	To reduce uncertainty of our results, we conduct our analysis by using a large model ensemble of 111 members. We also quantify the uncertainty contributions from different sources at a global scale. All the results confirm that our main conclusions are robust.
Blinding	Our data are collected from open access platform, and we have clearly illustrated our analysis at a global scale.

Did the study involve field work? ☐ Yes ☒ No

Reporting for specific materials, systems and methods

We require information from authors about some types of materials, experimental systems and methods used in many studies. Here, indicate whether each material, system or method listed is relevant to your study. If you are not sure if a list item applies to your research, read the appropriate section before selecting a response.

Materials & experimental systems

n/a	Involved in the study
☒	☐ Antibodies
☒	☐ Eukaryotic cell lines
☒	☐ Palaeontology and archaeology
☒	☐ Animals and other organisms
☒	☐ Clinical data
☒	☐ Dual use research of concern

Methods

n/a	Involved in the study
☒	☐ ChIP-seq
☒	☐ Flow cytometry
☒	☐ MRI-based neuroimaging